HHS Public Access

Author manuscript

Neuroscience. Author manuscript; available in PMC 2023 February 21.

Published in final edited form as:

Neuroscience. 2022 February 21; 484: 119–138. doi:10.1016/j.neuroscience.2021.11.021.

CA1 spike timing is impaired in the 129S inbred strain during cognitive tasks

Tolulope Adeyelu[1], **Amita Shrestha**[1], **Philip A. Adeniyi**[1], **Charles C. Lee**[1], **Olalekan M. Ogundele**[1]

[1]Department of Comparative Biomedical Sciences, Louisiana State University School of Veterinary Medicine. Baton Rouge, LA70803, Louisiana

Abstract

A spontaneous mutation of the disrupted in schizophrenia 1 (*Disc1*) gene is carried by the 129S inbred mouse strain. Truncated DISC1 protein in 129S mouse synapses impairs the scaffolding of excitatory postsynaptic receptors and leads to progressive spine dysgenesis. In contrast, C57BL/6 inbred mice carry the wild-type *Disc1* gene and exhibit more typical cognitive performance in spatial exploration and executive behavioral tests. Because of the innate *Disc1* mutation, adult 129S inbred mice exhibit the behavioral phenotypes of outbred B6 *Disc1* knockdown (*Disc1*$^{-/-}$) or Disc1-L-100P mutant strains. Recent studies in *Disc1*$^{-/-}$ and L-100P mice have shown that impaired excitation-driven interneuron activity and low hippocampal theta power underlie the behavioral phenotypes that resemble human depression and schizophrenia. The current study compared the firing rate and connectivity profile of putative neurons in the CA1 of freely behaving inbred 129S and B6 mice, which have mutant and wild-type *Disc1* genes, respectively. In cognitive behavioral tests, 129S mice had lower exploration scores than B6 mice. Furthermore, the mean firing rate (FR) for 129S putative pyramidal (pyr) cells and interneurons (int) was significantly lower than that for B6 CA1 neurons sampled during similar tasks. Analysis of pyr/int connectivity revealed a significant delay in synaptic transmission for 129S putative pairs. Sampled 129S pyr/int pairs also had lower detectability index scores than B6 putative pairs. Therefore, the spontaneous *Disc1* mutation in the 129S strain attenuates the firing of putative pyr CA1 neurons and impairs spike timing fidelity during cognitive tasks.

Keywords

Disc1; CA1; spike timing; firing rate; cortex; schizophrenia

Corresponding author: Ogundele OM, ogundele@lsu.edu, **Tel:** 225-578-9103, **Fax:** 225-578-9895.

Author contributions: OOM, AS, APA, and CL designed the experiments and performed the recording procedures. OOM, AS, AT, and PA analyzed the results. OOM, CCL, and AT prepared the manuscript. OOM and CCL verified the manuscript.

INTRODUCTION

The hippocampus is the brain region responsible for the processing of instantaneous memory during active recollection (Cho et al., 2012; Godsil et al., 2013; Li et al., 2015; Peyrache et al., 2012; Terada et al., 2017). In the CA1, excitatory synapses are formed on the dendritic spines of pyramidal (pyr) cells, and their plasticity is required for memory formation and retrieval (Bosch et al., 2014; Chazeau and Giannone, 2016; Hlushchenko et al., 2016; Lai and Ip, 2013; Nakahata and Yasuda, 2018; Penny and Gold, 2018; Penzes et al., 2011; Phillips and Pozzo-Miller, 2015; Stein et al., 2015). Therefore, genetic mutations or factors (environmental and chemical) that lead to spine dysgenesis in the CA1 produce significant cognitive symptoms that are associated with several developmental neuropsychiatric and degenerative neurological disorders.

The 129S and C57BL/6 mouse strains are among the most commonly used inbred strains in neuroscience research. Several transgenic mouse lines outbred from these parent strains are used to study synaptic plasticity, cognition, and neural circuits in the hippocampus-cortical circuits (and other circuits). Although these two strains have distinct genotypes and phenotypes, the 129S strain carries mutations that have profound effects on synaptic structure, plasticity, and cognitive performance. Notably, spontaneous mutation of the disrupted in schizophrenia 1 (*Disc1*) gene—which encodes DISC1, a structural protein at the excitatory postsynaptic density—results in behavioral phenotypes that recapitulate human schizophrenia and depression symptoms. In contrast, C57BL/6 mice carry the wild-type *Disc1* gene and have typical (wild-type) behavioral phenotypes.

Spontaneous mutation of the *Disc1* gene in 129S mice or engineered *Disc1* knockout in the C57BL/6 strain (B6:Disc1 *mut*) truncates the primary structure of the DISC1 protein, thus significantly impairing excitatory ionotropic and metabotropic glutamate receptor scaffolding at the postsynaptic density in the cognitive centers (Gomez-Sintes et al., 2014; Koike et al., 2006; Malavasi et al., 2018; Teng et al., 2018; Tomoda et al., 2016; Tropea et al., 2018; Tropea et al., 2016; Wang et al., 2011; Wexler and Geschwind, 2011; Zheng et al., 2011). Therefore, *Disc1* innate mutation in the 129S strain or induced mutation in B6 outbred strains (*Disc1* knock-in, knockdown, L100P) leads to a progressive loss of excitation and spine dysgenesis in the cognitive centers (Gomez-Sintes et al., 2014; Koike et al., 2006; Kvajo et al., 2008; Lee et al., 2011; Malavasi et al., 2018; Shao et al., 2017; Wu et al., 2013).

Although *Disc1* mutation primarily affects excitatory synapses, evidence suggests that the connectivity and firing rate of inhibitory γ-aminobutyric acid (GABA) neurons are influenced by abnormal DISC1 protein signaling. Genetic ablation of the *Disc1* gene in B6 mice leads to mossy fiber axonal mistargeting in the CA1, impaired GABAergic signaling, diminished counts of fast-spiking interneurons, and impaired inhibitory postsynaptic current in the hippocampus (Mesbah-Oskui et al., 2015; Sauer et al., 2015). Because of the broad effects of DISC1 protein on excitatory and inhibitory synaptic activity, various types of *Disc1* loss of function have been associated with the dysregulation of local hippocampal excitation, place cell function, and other related cognitive processes. Specifically, decreased resolution of the place field of CA1 place cells, suppressed hippocampal theta power, and erroneous gamma oscillations have been identified in other *Disc1* mutants but not the

129S strain (Mesbah-Oskui et al., 2015; Sauer et al., 2015). Together, the dysregulation of hippocampal (pyramidal) place cell firing and brain oscillations indicate a possible change in the pyramidal cell activation of interneurons in CA1 cognitive processes (Brown et al., 2020; Rebollo et al., 2018; Scheffer-Teixeira and Tort, 2016; Tiesinga et al., 2001).

Although the 129S inbred strain (with spontaneous *Disc1* mutation) and outbred B6 *Disc1* mutant strains show similar behavioral/synaptic phenotypes, previous studies on hippocampal function have focused on outbred B6 *Disc1* mutants. This research focus has created a major gap in the interpretation of neural circuit and computational outcomes of studies involving 129S mice and associated outbred strains (Clapcote and Roder, 2006; Gomez-Sintes et al., 2014). The current study provides evidence of the dysregulation of putative pyr cell firing and excitation-driven interneuron (int) activity in the CA1 in freely behaving 129S mice. Suppression of the putative pyramidal firing rate occurred across the intervals of hippocampal-dependent spatial exploration tasks and cortex-linked executive tasks (object exploration and sociability tasks). The mean firing rates of putative pyr cells in 129S CA1 ensembles were markedly lower than those of C57BL/6 pyramidal cells in similar tasks. Ultimately, analysis of pyr cell-interneuron pairs in 129S and C57BL/6 CA1 revealed a lower fidelity of spike timing for 129S putative pairs. These network changes were accompanied by lower exploratory propensity and sociocognitive decline in the 129S inbred strain.

METHODS

Experimental animals

C57BL/6 (JAX:000664) and 129S (JAX:002448) breeding pairs were acquired from Jackson Laboratories (Bar Harbor, ME, United States). Mice were housed in a temperature-controlled environment at 22 ± 1°C with alternating 12-hour light and dark cycles. Food and water were provided ad libitum. Mice without implants were housed in groups of five per cage. Animals with neural implants were housed individually to prevent damage to the neural probes. Occasionally (two or three times per week), the animals interacted with other mice in laboratory settings to mitigate social isolation. All procedures performed in this study were approved by the Institutional Animal Care and Use Committee of the Louisiana State University School of Veterinary Medicine.

Genotyping of the *Disc1* mutation in the 129S strain

Tail tissue (2 mm) was collected from postnatal day 15 mice (129S and C57BL/6) and lysed with DirectPCR lysis reagent (#101-T, Viagen biotech). 1 μg of DNA in crude lysate containing Dreamtaq green PCR master mix (#K1081, Thermo Scientific) was amplified in a thermocycler. Subsequently, 10 μL of the PCR product was electrophoresed at a constant voltage of 100 V for 30 mins through ethidium bromide-stained 1% agarose gel. The incubation reaction conditions for the *Disc1* primers, 5′-TAG CCA CTC TCA TTG TCA GC-3′ (forward) and 3′-CTC CAT CCC TTC CAC TCA GC-5′(reverse) were obtained from the literature (Gomez-Sintes et al., 2014). A 25-bp deletion mutant allele (129S) and the wild-type allele (C57BL/6) were distinguished by bands at 179 bp and 196 bp, respectively (Figure 1A).

Spine dysgenesis and transmission electron microscopy (TEM)

Spine dysgenesis, a notable phenotype in 129S CA1 synapses, was visible by TEM on postnatal day 60 (Figure 1B). Tissue processing and imaging for TEM were as previously described (Ogundele and Lee, 2018; Shrestha et al., 2019). In brief, microdissected hippocampus tissue was fixed in a mixture of 1.6% paraformaldehyde, 2.5% glutaraldehyde, and 0.03% $CaCl_2$ in 0.05 M cacodylate buffer (pH 7.4). Rapid fixation was performed for 2 h at room temperature and thereafter at 4°C. In-block staining of the hippocampus was performed with 2% uranyl acetate. Subsequently, the tissue was dehydrated in alcohol and polymerized for 24 h at 60°C. Images were acquired with a JEOL 1400 TEM microscope equipped with a GATAN digital camera. Typical synapses were identified by the presence of presynaptic vesicles, postsynaptic density, and postsynaptic mitochondria.

Electrode implantation

Adult 129S (n=4) and C57BL/6 mice (n=4) weighing ~25 gm were used for this study. Mice were anesthetized through intraperitoneal injection of a ketamine/xylazine cocktail (100 mg/kg and 10 mg/kg, respectively). After the plane of anesthesia was established, a toe pinch test was performed to verify the absence of sensation. Mice were fixed on a multi-rail stereotactic frame (Kopf Instruments, CA) for craniotomy procedures. The AP (−1.94 mm) and ML (1.2 mm) coordinates of the hippocampus were determined with an ultrafine hydraulic micromanipulator (1 μm resolution, Narishige, Japan). A 2 mm × 2 mm craniotomy was performed on the skull at this location. A ground screw was positioned in the occipital bone and connected to a ground wire. With a probe holder mounted on a hydraulic micromanipulator, four-channel microelectrode arrays (Microprobes Life Sciences, MD) or four-channel silicon probes (Neuronexus, MI) were positioned dorsoventrally in the CA1 pyramidal layer at 1.1 mm depth (DV) from the pial surface of the brain. Before the implantation, neural probes were connected to a pre-amplifier head stage tethered to a recording controller (Intantech, USA). This allowed for the detection of spontaneously evoked neural spikes in the CA1 with the upper and lower cut-off frequencies set at 300 Hz and 5,000 Hz, respectively. After the final depth was established, the location of the electrode contact site was adjusted by ±50 μm, along the DV axis to optimize the detection of extracellular spikes. With the probes in position, the ground wire and craniotomy were covered with orthodontic resin. Adequate postoperative care was given. After 7 days of recovery, the fidelity of the electrode channels was determined through sample recordings and impedance measurements. For all viable channels, the impedance ranged from 0.5 to 5 megΩ. On average, the implanted electrodes were structurally stable and recorded reliable impedance scores for ~6 months (Figure 1C). For this experiment, we used recordings obtained no more than 4 months after the electrode implantation. At the end of the experiments, the electrode implantation tract (recording site) was verified with DAPI fluorescence (Figure 1D–E).

Behavioral tasks with in vivo electrophysiology—Mice were acclimated to the behavioral testing room and an open field chamber for 5 days before the behavioral tests. Behavioral testing session data were acquired and analyzed in Ethnovision XT15 (Noldus) software. Baseline cognitive performance was determined in a set of naïve B6 (n=7) and 129S (n=6) mice without cranial implants. A separate set of B6 (n=4) and 129S (n=4)

mice with long-term implants were tethered for neural recording during modified behavioral tasks. For all behavioral tasks, mice with implants were acclimated to the testing chamber with tethers and head stage connections (Figure 1C).

Spatial exploration of an open field: Mice were placed in an open field and explored the chamber for 5 minutes. During the exploration task, the velocity (cm/s) and distance covered (cm) by the mice were detected with behavioral tracking software (Ethovision XT15, Noldus). For mice with neural implants, extracellular spikes were recorded throughout the 300-sec duration of the test. Because 129S mice are generally less active than B6 mice, behavioral parameters for the test duration were rendered in 30-sec bins to detect the periods of exploratory activity. In subsequent analysis, three 30-sec bins with exploratory events were selected for the 129S mice. Analysis of the putative unit change in firing rate (ΔFR, spikes/sec) during exploration of an open field was performed with neural spikes sampled around the selected active periods (90 sec). To determine the mean firing rate (Hz) of putative neurons in spatial exploration events, we sampled neural spikes for intervals with >10 sec of continuous movement at a speed of ~1.5 cm/s, over a 15-sec duration.

Novel object recognition test and object exploration: B6 and 129S mice without neural implants explored an open field chamber (5 mins) with similar objects (x1 and x2) located at two separate positions (A, B). After a 25 minute intertrial time, a novel object (y) replaced the familiar object (x2) at position (B) for the acquisition trial (5 minutes). Here, we determined the count of object contacts for x1/A and y/B. For executive memory function (object recognition), we expected that the mice would show a preference for the novel object. For mice with neural implants/tethers, 30-sec bins with an exploratory speed of ~1.5 cm/s were selected for the analysis of putative unit ΔFR (spikes/sec). Furthermore, the mean FR (Hz) of putative units was determined from spike events sampled during intervals with at least four object exploration events. An object exploration event was defined as a combination of a 5-sec interval before object contact, nose-point reaching for an object (~3–5 sec), and a 5 sec interval sec after withdrawal of the noise-point.

Sociability test: A three-chambered test was used to assess social interaction behavior in B6 and 129S mice without neural implants. After each mouse acclimated to the test chamber, a stranger mouse (S1) was placed in one of the holding compartments. For sociability tests, we expected that normal mice would show a preference for the stranger mouse rather than the empty chamber (E).

CA1 extracellular voltage recording in mice with implants was performed in a modified sociability test. A single holding compartment containing a stranger mouse (S_1) was positioned in the middle of the test chamber. As described above, social interaction was defined as nose-point reaching for the stranger mouse in the holding compartment. Neural recording and sociability tests for B6 and 129S mice were performed for 300 sec. The velocity of movement was also assessed in 30-sec bins to determine intervals with exploratory activity for 129S mice. For subsequent analysis of ΔFR for putative units, 30-sec bins with a ~1.5 cm/s velocity were selected for the less active 129S mice. However, for the assessment of the mean FR of putative units, a social contact event was determined as follows: 5 sec before social contact, social contact period (~3–5 sec), and 5 sec after social

contact (~15 sec). For a 300 sec test, intervals with at least four social contact events were used to determine the mean FR scores.

Summary of experimental sessions: The combined behavioral task and *in vivo* electrophysiology sessions used in this study were as follows: 129S_mouse 1 (spatial: 4, object exploration: 3, sociability: 3), 129S_mouse 2 (spatial: 2, object exploration: 3, sociability: 3), 129S_mouse 3 (spatial: 2, object exploration: 3, sociability: 2), 129S_mouse 4 (spatial: 3, object exploration: 5, sociability: 4), C57BL/6_mouse 1 (spatial: 2, object exploration: 4, sociability: 0), C57BL/6_mouse 2 (spatial: 2, object exploration: 7, sociability: 2), C57BL/6_mouse 3 (spatial: 3, object exploration: 6, sociability: 3), and C57BL/6_mouse 4 (spatial: 3, object exploration: 0, sociability: 3).

Spike sorting and single unit detection—Extracellular spikes (μV) were continuously sampled from the CA1 of B6 and 129S mice during behavioral tasks. In Plexon Offline Spike Sorter (OFSS), extracellular spikes were pre-processed with a Butterworth filter (300–5,000 Hz) to remove anatomical drift and local field potential artifacts. Single unit clustering of the recorded spike was performed with principal component analysis (PCA) to detect putative neurons (single units). To improve the signal-to-noise ratio, we used an amplitude discrimination step in the OFSS. A lower peak crossing threshold of 5× the root mean square was set for each electrode channel to eliminate noise and cross-channel artifact spikes (Chung et al., 2017; Quiroga, 2012; Swindale et al., 2017). Where necessary, unsorted spikes were manually invalidated in the OFSS. Because more than one putative unit was detected on each electrode channel, spikes were further discriminated against based on the interspike interval (ISI). Thus, for two spikes to be assigned to the same putative unit, an ISI >1 ms was necessary. This step accounted for the refractory period in action potential and prevented ISI violation (Chung et al., 2017; Quiroga, 2012). Post-processing overlap analysis (splitting and merging) was performed in Spikesorter software (Swindale et al., 2017). Subsequently, waveforms of clustered units were inspected across all channels. Viable units were accepted based on the autocorrelogram and crosscorrelogram plots, firing rate, and ISI distribution. Putative pyr cells had peaked autocorrelograms, whereas int had troughed autocorrelograms in plots of the number of events per unit time with 0.5 ms bin resolution. Through ISI characterization methods, extracellular action potentials were characterized as spikes (two spikes in >7 ms) or bursts (two or three spikes in <7 ms).

Statistics

Statistical analyses were performed in Neuroexplorer and OriginPro 2021b software. Kolmogorov-Smirnov tests were performed to determine the normality of the data set (α=0.05). Mann-Whitney U tests or T-tests were used to compare behavioral task performance or electrophysiological outcomes for B6 and 129S mice. Kruskal-Wallis ANOVA or one-way ANOVA was performed to compare the putative unit mean firing rate and CCH connectivity lag across the three behavioral tasks. Repeated measures ANOVA and chi-square (chi-sq) tests were performed to determine whether the change in firing rate (ΔFR) and the velocity (Δcm/s) were significant for consecutive experimental intervals (bins). Correlations between electrophysiological parameters were determined

with Pearson's (r) method. A two-tailed test of significance (α=0.05) was used. Pearson's correlation outcomes are presented as marginal histograms.

RESULTS

Experimental intervals for CA1 recording in freely behaving mice

The putative neuron firing rate was determined in two ways for each behavioral task. First, a change in firing rate (ΔFR, spikes/sec) was determined for putative neurons during the exploratory behavior associated with each task. Second, task-specific events such as object or social contact were used as references for determining the mean FR (Hz) of putative units. A 300-sec task duration is standard in rodent cognitive-behavioral tests (Brown et al., 2020; Kaidanovich-Beilin et al., 2011; Wolf et al., 2016). Although the B6 mice routinely performed behavioral tasks and explored the test chambers, the 129S mice were less active. Thus, to assess the exploration propensity and ΔFR of putative units during spatial exploration, object exploration, and social interaction tests, we assessed task performance in 30-sec bins to detect the periods of behavioral activity for 129S mice (ten bins). For 129S mice, three bins (90 sec) with ~1.5 cm/s exploration velocity were selected. To determine the ΔFR, we further segmented selected bins with exploratory activity (three bins or 90 sec) into six 15-sec bins.

Because of the irregular exploratory behavior of 129S mice, the mean FR (Hz) of putative neurons was determined from intervals that contained at least four task-specific events. The following events were considered for the behavioral tasks: (i) **Spatial exploration:** continuous movement at a velocity ~1.5 cm/s for ~10 sec over a 15-sec duration. At least four events were detected for a typical 129S mouse in an open field test session. (ii) **Object exploration:** the time of nose-point exploration of an object (T_0) was used as the reference with 5 sec before and 5 sec after the reference event. (iii) **Social contact:** the time of nose-point exploration of stranger mouse holding compartment (T_0) was taken as the reference with 5 sec before and 5 sec after the reference event. Movie 1 and Movie 2 demonstrate chronic neural recording in a freely behaving mouse during spatial and object exploration tasks. Here, center-body tracking was used to plot the animal trail (time lag, 10 sec).

Characterization of B6 and 129S CA1 putative pyr and int units

The viability of electrode channels positioned in the CA1 was determined with impedance measurements and the identification of neuronal ensembles detected on electrode channels (Figure 2A). Single unit clusters were detected with PCA of continuously recorded CA1 extracellular spikes. Figure 2A shows samples of putative unit clusters detected in a mouse CA1 10 days and 30 days after electrode implantation (day 0). To distinguish between putative pyr cells and int, the shape of the autocorrelogram (ACG, 0.5 ms bin), firing rate (Hz) distribution of the putative units, ISI range scores, and waveform shapes were used. Putative units with distinct ACG peaks at 0 ms followed by a rapid decay (50 ms) were characterized as putative pyr cells (Figure 2B). Int ACGs showed a distinct trough at 0 ms, with sustained activity (Figure 2C). Interneurons were further distinguished from pyramidal cells by higher FR scores and the absence of complex spiking (Figure 2D; $p<0.0001$).

Putative units identified as pyr cells (B6: n=332, 129S: n=194) exhibited a mean FR of ~5 Hz, whereas the int FR ranged from 8 to 40 Hz (B6: n=590, 129S: n=495). In addition, putative int exhibited significantly lower ISI than the pyr cells in B6 (Figure 2E, $p<0.0001$) and 129S (Figure 2F, $p<0.0001$) CA1 neuronal ensembles. Notably, the 129S pyr and int mean ISI scores were also significantly higher than those of B6 pyr (Figure 2G, $p<0.0001$) and int (Figure 2H, $p<0.0001$) units. PCA clustering of waveforms demonstrated a distinct energy distribution for putative pyr and int units in three-dimensional space (Figure 2I). Clustered spikes for putative interneurons had a shorter duration of action potentials (spike width, μsec) than the pyr cell waveforms (Figure 2J). Fewer viable pyramidal neurons were detected in 129S than B6 CA1 across all experimental sessions (Figure 2D). Ultimately, neurons with ambiguous or overlapping pyr/int features were excluded from the analysis.

Comparative cognitive performance of B6 and 129S mice

The hippocampus encodes working and spatial memory for instantaneous recollection. Neural circuits between the hippocampus and prefrontal cortex govern executive behavior such as object discrimination and social memory (Basu and Siegelbaum, 2015; Funahashi, 2017; Funahashi and Andreau, 2013; Jin and Maren, 2015; Li et al., 2015; Lueptow, 2017; Nadel and Hardt, 2011; Ranganath et al., 2005; Spellman et al., 2015; Wolf et al., 2016). Here, we compared the CA1 putative neuron firing rate and pyr/int connectivity profile for inbred B6 and 129S mice during cognitive tasks.

Open field and spatial exploration tasks

Because the 129S strain has a lower exploratory propensity than the B6 strain, we assessed how the neural implants/tethers affected exploratory behavior in both strains. To determine the effects of the implants/tethers on movement, we examined the mean velocity (cm/s) and distance (cm) for the B6 and 129S groups in open field tasks. The results indicated significantly lower mean distance (Figure 3A; $p<0.0001$) and velocity (Figure 3B; $p<0.0001$) for B6 mice with implants/tethers (n=4) than without implants (n=10). B6 mice without neural implants/tethers had a mean velocity score of ~7 cm/s, compared with a ~3.5 cm/s score for B6 mice with implants/tethers. Similarly, the mean distance for B6 mice was 170 cm without neural implants and ~105 cm with implants/tethers. Interestingly, the mean distance (Figure 3C; $p=0.13$) and velocity (Figure 3D; $p=0.21$) did not change significantly for 129S mice with and without implants/tethers (~60 cm and ~1.5 cm/s, respectively). From these results, we concluded that the lower exploration propensity in 129S mice was phenotypic, such that the mean distance and velocity were at least 2-fold lower than those in the B6 strain. In support of this outcome, a comparison of the mean distance (cm) and velocity (cm/s) for mice with implants (B6 and 129S; Figure 3E) during open field tasks revealed significantly lower scores for the 129S group (Figure 3F and G; $p<0.0001$). Similarly, the mean velocity for the 129S mice was significantly lower than that for the B6 mice with implants/tethers (Figure 3H; $p<0.0001$).

The tracking of mouse body movement showed that 129S mice, compared with B6 mice, were less active. This was evident as a shorter duration of body movement (Figure 3I; $p=0.002$), and prolonged duration of inactivity (Figure 3J; $p<0.0001$) in open field tasks (Figure 3K). 129S mice also had significantly lower mobile states than the B6 mice (Figure

3L; p<0.0001). Notably, 129S mice avoided the center square of the open field chamber and were active mostly around the edges (Figure 3G and 3K). In contrast, B6 mice routinely explored the central area and edges of the chamber. This finding is likely to indicate anxiety in the 129S strain, although that topic is beyond the scope of the current study.

Assessment of the change in velocity (Δcm/s) across 30-sec bins of the open field task indicated that the velocity of exploration did not change significantly for the B6 group (Figure 3M, chi-sq=0.43; p=0.6). In contrast, 129S mice had lower velocity scores during the intervals (bins) of open field tasks (chi-sq=4.2; p=0.04). Furthermore, the 129S Δcm/s scores per 30-sec bins were also significantly lower than the B6 scores (p<0.0001).

The putative CA1 unit FR (mean) in spatial exploration events was considered for intervals with ~1.5 cm/s velocities that were sustained for ~10 sec over a 15 sec period (Figure 3N–O). The mean FR (Figure 3P; p<0.0001) and burst discharge rate (Figure 3Q; p<0.0001) for 129S putative pyr cells (n=64) were significantly lower than those for B6 pyr cells (n=79). Because putative pyr FR is strongly correlated with the exploration speed, the low velocity scores for 129S mice were accompanied by significantly lower FR scores for the intervals of the task (two-way ANOVA, p<0.0001). For the selected 90-sec bin with exploratory activity, the ΔFR was not significant for B6 (Figure 3R; chi-sq=0.162; p=0.69) or 129S (chi-sq=0.16; p=0.67) pyr cells.

The mean FR of 129S putative int (n=123) was significantly lower than the B6 int FR scores (n=126) (Figure 3S; p=0.02). As observed for pyr cells, the ΔFR spread (spikes/sec) for B6 (chi-sq=0.28; p=0.59) or 129S (chi-sq=0.04; p=0.84) putative int did not change significantly for the intervals of open-field exploration tasks. Likewise, no significant difference was observed in firing rate change for B6 and 129S putative int across the intervals of the spatial exploration tasks (Figure 3T). Together, the results showed that 129S putative pyr cells and interneurons had lower firing rates (Hz) than B6 neurons in a hippocampus-dependent spatial exploration task.

Object recognition and exploration

Executive cognitive performance was first determined for mice without neural implants (B6, n=5; 129S, n=4) through a novel object recognition test. Compared with the B6 mice, the 129S mice showed minimal object exploration propensity, as evidenced by a lower frequency of object contact (Figure 4A–B; p=0.02). Because the frequency of total object contact was significantly lower (<5 events) in the 129S group, the memory index (object discrimination) could not be computed. With low object exploration propensity, animals are unlikely to learn tasks sufficiently to discriminate between objects. This was evident as significantly lower distance (Figure 4C, p<0.0001) and velocity (Figure 4D, p<0.0001) scores for naïve 129S mice in object recognition tests.

B6 mice with neural implants (Figure 4E) exhibited lower exploration velocity and distance than mice without implants (Figure 4F; p<0.0001, p<0.0001) in object exploration tests. Similarly, no significant change was observed in exploration velocity and distance for 129S mice with or without implants in object exploration tasks (Figure 4G; p=0.23, p=0.23). Although 129S mice with implants had lower exploration propensity than B6 mice (Figure

4H), object exploration occurred during some of the active intervals, such that the frequency of object contacts per active 30-sec bins was not significantly different from the B6 scores (Figure 4I; p=0.33). Because of their lower exploration propensity, 129S mice were intermittently immobile around the object zone (cm radius around the object edge) and thus had a significantly higher duration around objects (Figure 4J–K, p=0.01). The exploration distance (Figure 4L; p<0.0001) and velocity (Figure 4M; p<0.0001) were significantly lower for 129S mice in object exploration tasks.

In subsequent analyses, the mean firing rate was determined for B6 and 129S putative units for object contact events (Figure 4N). Intervals with at least four object contact events were considered for each B6 or 129S mouse in the analysis of putative neuron mean FR (Figure 4O). Although the velocity for B6 (chi-sq=1.7; p=0.19) and 129S mice (chi-sq=0.79; p=0.37) did not change significantly, the B6 scores were significantly higher than the 129S velocity for all intervals (Figure 4P; two-way ANOVA, p<0.0001). The lower exploration velocity in object recognition tasks for 129S mice was accompanied by significantly lower mean FR (Figure 4Q; p<0.0001) and burst rate scores for the pyr units (n=69) than those for B6 pyr (n=216) cells (Figure 4R; p<0.0001). ΔFR analysis of B6 pyr units revealed a significant decrease during the 90-sec intervals with exploratory activity (Figure 4S, chi-sq=4.66; p=0.03). Together with lower exploration Δcm/s (Figure 4P), the ΔFR for 129S putative pyr cells significantly declined over the 90-sec interval (six 15-sec bins) with ~1.5 cm/s velocity (chi-sq=24.9; p<0.0001). However, the firing rate of 129S pyr cells was significantly lower than the B6 FR scores for all bins considered (Figure 4S; two-way ANOVA, p<0.0001).

The mean FR of 129S putative int was significantly lower than the B6 int scores (Figure 4T; p=0.006). Interestingly, ΔFR analysis of B6 (n=359) and 129S (n=239) int units for intervals with exploratory activity revealed a similar firing rate spread. Both B6 (chi-sq=0.34; p=0.89) and 129S (chi-sq=3.82; p=0.051) int exhibited steady firing rate ranges for the 90-sec duration of exploration (Figure 4U). Likewise, no significant difference was observed between B6 and 129S ΔFR scores for the six 15-sec bins with exploratory activity (two-way ANOVA, p=0.61). Together, the results showed that putative 129S putative pyr and int mean FR were significantly lower than B6 FR scores for object exploration events. However, similar patterns were observed for ΔFR across intervals with exploratory activity. Specifically, B6 and 129S pyr cells showed a decrease in firing rate with time, whereas putative int units had sustained FR scores.

Social interaction behavior

A three-chambered test was performed to assess social interaction in B6 and 129S mice without neural implants (Figure 5A). As expected, B6 mice showed a significant preference for the social mouse (S1) rather than the empty chamber E (Figure 5B, p=0.0017). In contrast, for 129S mice, no significant difference was observed between the time spent exploring E or S1 (Figure 5B, p=0.351). Together, the sociability index, i.e., the percentage of time spent exploring the social mouse [S1/(S1+E)], was significantly lower for the 129S than the B6 group (Figure 5C, p=0.002). In agreement with this outcome, 129S mice showed lower chamber exploration propensity (Figure 5D), as evidenced by significantly lower

distance (Figure 5E; p<0.0001) and velocity (Figure 5F; p<0.0001) scores than those of the B6 mice.

To sample CA1 spikes during sociability tests, we used a modified setup with a single stranger mouse enclosure (Figure 5G). Similar to the findings in the open field and object exploration tasks, B6 mice with implants had lower distance (p<0.0001) and velocity (p<0.0001) scores than did mice without implants (Figure 5H). Likewise, the exploration distance (p=0.30) and velocity (p=0.38) did not differ in 129S mice with or without neural implants (Figure 5I). Similar to naive 129S mice (Figure 5C), tethered 129S mice had fewer social contacts with the stranger mouse than tethered B6 mice(Figure 5J–K; p=0.014). In support of these outcomes, the exploration distance (Figure 5L; p<0.0001) and velocity (Figure 5M; p<0.0001) for tethered 129S mice were significantly lower than those for tethered B6 mice in sociability behavioral task sessions with neural recording.

Based on the outcomes of behavioral tasks, we subsequently compared the mean FR and ΔFR for B6 (n=39) and 129S (n=61) putative pyr neurons for intervals with significant social contacts (Figure 5N–O) and exploration of the sociability test chamber (Figure 5P), respectively. For the duration of the task (300 sec), no significant change was observed in velocity for B6 (chi-sq=0.076; p=0.78) or 129S (chi-sq=1.22; p=0.27) mice. However, the 129S velocity scores were significantly lower than those of the B6 group (two-way ANOVA, p<0.0001).

We observed that 129S pyr cells had a significantly lower mean FR (Figure 5Q; p=0.005) and burst rate (Figure 5R; p<0.0001) for social contact events than B6 pyr cells. B6 putative pyr cells showed a significant change in firing rate for the intervals with exploratory activity (Figure 5S, chi-sq=5.3; p=0.03). No significant change was observed in the firing rate for 129S pyr cells (chi-sq=0.8; p=0.37). Of note, for all intervals with significant exploratory activity, the B6 pyr cell FR scores were significantly higher than the 129S pyr cell mean FR (two-way ANOVA, p<0.0001).

129S putative int (n=133) mean FR was significantly lower than the B6 (n=105) int scores (Figure 5T; p<0.0001). For the intervals with exploratory activity, the firing rate for 129S int was also significantly lower than the B6 firing rate scores for similar intervals (Figure 5U; two-way ANOVA, p<0.0001). A change in the 129S int firing rate spread was observed in the period of exploratory activity (ΔFR, chi-sq=5.1; p=0.023). In contrast, B6 putative int firing rate did not change significantly for the intervals with exploratory activity during the sociability tests (ΔFR, chi-sq=1.7; p=0.19).

Summary of firing rate analysis of behavioral tasks

Together, the outcomes of firing rate analysis in 129S and B6 CA1 ensembles indicated that a decrease in 129S mice exploratory activity was probably associated with the lower pyr cell and int firing rate. Interestingly, the change in firing rate for the period of exploration (90 sec) revealed task-specific alterations in the 129S group. In the hippocampus-dependent spatial exploration task (open field), B6 and 129S showed similar ΔFR patterns, such that no significant changes were found in FR spread for the period of exploratory activity (pyr; Figure 3R and int, Figure 3T). In the object exploration tasks, B6 and 129S putative units

also recorded similar ΔFR patterns. Both B6 and 129S putative neurons showed a significant decrease in firing rate (Figure 4S), whereas putative int units showed no significant change in FR during intervals with exploratory activity (Figure 4U). However, for exploration intervals during sociability tests, 129S pyr and int units showed ΔFR patterns that differed from those of B6 neurons sampled during similar tasks. The ΔFR of B6 pyr cells decreased significantly across sociability test intervals, whereas 129S ΔFR showed no change across similar intervals (Figure 5S). In contrast, B6 int ΔFR showed no significant change during exploratory events in sociability tasks, whereas the 129S int firing rate decreased across the same intervals of chamber exploration (Figure 5U).

Firing irregularity in 129S putative neurons

In addition to the characterization of putative units based on their FR (Hz), we further assessed the distribution of the units by plotting the mean FR and ISI scores. Through this method, previously characterized pyr and int units were clustered in edge histograms (Figure 6A–B). B6 and 129S putative pyr cells showed significant variability in mean ISI scores and a narrow range of mean FR (Hz). In contrast, putative int units had a narrow ISI range with significant FR variability (Figure 6A–B). Therefore, to compare the firing regularity for B6 and 129S putative pyr cells or interneurons, we considered both FR- and ISI-dependent indices. The firing regularity of putative neurons, which is dependent on the firing rate (n/t), was determined as the coefficient of variation (CV) of ISI (σ_{ISI}/ISI_{mean}). ISI-dependent firing regularity was assessed with the more stringent CV2 score. Thus, we expected that ISI variability in putative pyr cells would lead to a change in CV2, and the firing rate variability of putative interneurons would be likely to alter the CV score (Arancillo et al., 2015; Brischoux et al., 2009; Ponce-Alvarez et al., 2009; Ponce-Alvarez et al., 2010; Prescott and Sejnowski, 2008; Suresh et al., 2016). However, for putative units with extreme firing irregularity, both the CV and CV2 scores might be affected.

In the hippocampus-dependent spatial exploration task (open field), 129S putative pyr cells exhibited significantly higher CV2 scores than those for B6. This outcome suggested significant variability in ISI, but not FR, and decreased firing regularity for 129S putative pyr cells (Figure 6C; CV $p=0.92$, CV2 $p<0.0001$). In contrast, the FR variability was robust in putative int; thus, a comparison of 129S and B6 int units revealed a higher CV score for 129 interneurons. For 129S int units, the significant FR variability appeared to underlie the lower firing regularity score (Figure 6D; CV $p<0.0001$, CV2 $p=0.44$).

It follows that executive behavioral tasks that involved cortical activation improved firing regularity for putative pyr cells and not int units in 129S CA1 ensembles. In object exploration tasks, the CV and CV2 scores did not significantly differ between 129S and B6 pyr cells (Figure 6E; CV $p=0.11$, CV2 $p=0.053$). However, 129S int showed significant FR variability, indicated by higher CV scores than those of B6 int in object exploration tasks (Figure 6F; CV $p<0.0001$, CV2 $p=0.96$). Similarly, in sociability tests, the CV and CV2 scores did not significantly differ between 129S and B6 pyr cells (Figure 6G; CV $p=0.65$, CV2 $p=0.168$). In sociability tasks, the FR and ISI variability were significant for 129S putative interneurons. Therefore, the CV and CV2 scores were significantly higher for 129S int units than the B6 scores (Figure 6H: CV, $p<0.0001$; CV2, $p=0.001$). These

outcomes suggested that the ISI variations observed for 129S putative pyr cells during hippocampus-dependent tasks significantly normalized during executive behavioral tasks involving cortical activation. For cortex-dependent tasks, the pattern of putative CA1 int firing irregularity also varied in object exploration and sociability tasks. Although significant FR variability was recorded for 129S int in object exploration tasks, variability in both FR and ISI was observed in sociability tasks.

Putative CA1 pyr/int synaptic connections

Given that 129S putative pyr cells and int had significantly lower FR and firing regularity, we sought to ascertain the fidelity of pyramidal cell-driven interneuron activity in the CA1 of 129S mice during the various behavioral tasks. This was important because of the role of pyr/int pairing on hippocampal oscillations, which is pertinent to information encoding and cognition. Anatomically, a diverse population of interneurons ($GABA^+$) is in the oriens, pyramidal cell, and radiatum layers of the CA1. Figure 7A illustrates the distribution of $VGAT^+$ interneurons in the hippocampus, and their anatomical dominance in the pyr cell layer, the recording site. As described previously, putative interneurons in CA1 ensembles were characterized by their firing rate, ISI, and waveform (Figure 2B–J). Putative pyr cells and interneurons detected on electrode contact sites carried on a single shank were used for subsequent analysis of pyr/int synaptic connections.

The decline in spatial exploration velocity, object exploration, and sociability contact for 129S mice are indicative of cognitive decline potentially resulting from either decreased interneuron activation and (or) low pyr cell firing (Bohbot et al., 2017; Buzsaki, 2002; Godsil et al., 2013; Mizuseki and Buzsaki, 2014; Woldeit and Korz, 2010; Yamaguchi et al., 2004). To assess the fidelity of putative pyr/int pairs in CA1 ensembles, we combined putative neuron ACGs to create crosscorrelograms (CCH, 0.5 ms bins) for short-latency interactions. CCH peak lag (ms) was used to characterize synaptic connections for B6 and 129S putative pyr/int pairs. Based on previously established methods (Bartho et al., 2004; Diba et al., 2014; Kobayashi et al., 2019; Pastore et al., 2018), reference pyr and target int pairs with positive CCH peak lag indicate pyr (excitation) activation of the int targets. In contrast, a negative or dual peak indicates feedback inhibition of a reference pyr cell after activation of the target interneuron (reverberating connection). Peaks aligned at 0 ms lag represent neurons with a common presynaptic input. Pairs with common presynaptic inputs were characterized by a peak lag of less than 1.4 ms. Monosynaptic pyr/int pairs showed CCH peaks with a lag time between 1.5 and 5 ms. Multi-synaptic connections had CCH peaks greater than 5 ms. We set the maximum time for multisynaptic connections to 30 ms because the maximum interelectrode distance is 50 μm within the CA1 pyr cell layer.

Although the B6 pyr mean FR was significantly higher than the 129S pyr scores, variations in FR also occurred between hippocampus-linked and cortex-dependent behavioral tasks. The mean FR for B6 putative pyr units in spatial exploration events was significantly higher than the FR score for object exploration (Figure 7B; p=0.02) and social interaction events (p=0.05). In contrast to the observation for B6 pyr cells, the FR for 129S pyr cells in spatial exploration events was either not significant or significantly lower than the FR for executive tasks (Figure 7C; obj: p=1, soc: p=0.01). Interestingly, for hippocampal and cortical tasks,

no significant difference was observed between the interneuron firing rates sampled in B6 (Figure 7D) and 129S (Figure 7E) neuronal ensembles. Together, these results indicated that the dysregulation of excitability (i.e., low pyr FR score) in the 129S CA1 might underlie some of the observed behavioral and cognitive phenotypes in the 129S strain.

Given that pyr excitation is pertinent to int activation, we determined whether the low FR of 129S pyr cells might affect CA1 pyr/int putative connections. We compared the normalized distribution of connection types (%) for B6 and 129S CA1 ensembles during behavioral tasks (Figure 7F). The B6 pyr/int putative pairs sampled for CA1-dependent spatial exploration tasks (n=132 putative pairs) showed predominantly monosynaptic (< 5 ms, 35.4%) and transsynaptic (5.1-14.5ms, 43.3%) connections (Figure 7G). Subsequent analysis of the connectivity profile for cortex-dependent executive tasks revealed a significant delay in pyr/int CCH peak lag. Consequently, the distribution of monosynaptic pairs in B6 CA1 ensembles decreased to 11.1% and 3.3% for the object (n=324 putative pairs) and sociability (n=96 putative pairs) tasks, respectively. In addition, the distribution of pyr/int pairs with transsynaptic and delayed CCH peak lag increased during object exploration and sociability tasks compared with spatial exploration tasks. The transsynaptic (5.1-14 ms) and delayed connections (>15ms) increased from spatial task scores of 43.3% and 4.7%, respectively, to (i) object exploration: 52.9% and 23.5%, respectively, and (ii) sociability: 50% and 34.8%, respectively.

Characterization of putative pyr/int connections based on CCH peak lag revealed similar outcomes for B6 and 129S CA1 ensembles. However, 129S ensembles contained a higher percentage of putative pairs with reverberating connections (Figure 7H–I; spt: n=94, obj: n=143, soc: n=119). The normalized distribution of monosynaptic pairs with positive CCH peak lag in 129S ensembles was significantly lower for the cortex-linked executive behavioral tasks (obj: 14.5%, soc: 4.4%) than the spatial task (29.2%). This distribution pattern was similar to the B6 pyr/int connectivity profile (spatial: 35.4%, obj: 11.1%, soc: 3.3%) (Figure 7I). Together, the results indicated that cortex-dependent behavior involved a delay in CA1 pyr/int connection. Notably, the sociability test produced the most significant decrease in the distribution of monosynaptic pairs (<5 ms) in both strains (B6: 3.3%, 129S: 4.4%). In agreement with these results, the distribution of putative pairs with transsynaptic (5.1-15 ms) and delayed connections (>15ms) increased during the object and social exploration tasks. The 129S CA1 ensembles contained 28.1% of transsynaptic pairs and 25.8% of pairs with delayed connection during spatial exploration tasks. Interestingly, these connection types increased in 129S CA1 ensembles for object exploration (obj: 40.5%, soc: 30.5%) and sociability (obj: 46.5%, soc: 42.1%) tasks, respectively.

Subsequent comparison of the mean CCH peak lag showed a significant delay in connection time for 129S pyr/int pairs during spatial exploration tasks, when compared with the B6 score (Figure 7J; p=0.007). For cortex-linked object exploration tasks, the 129S CCH peak lag did not significantly differ with respect to that in the B6 pyr/int pairs (Figure 7K; p=0.34). In contrast, 129S putative pairs showed a significantly prolonged CCH peak lag when sampled during sociability tasks (Figure 7L; p=0.04).

Comparison of the CCH peak lag for B6 putative pairs revealed variation in the mean lag across behavioral tasks. Specifically, putative pairs sampled in spatial exploration tasks had a mean lag significantly lower than those in the object exploration (Figure 7M; $p<0.0001$) and sociability tasks ($p<0.0001$). These outcomes were consistent with the percentage distribution of pyr/int connection types. Specifically, the distribution of monosynaptic putative pairs was highest during the spatial exploration task and decreased for the object exploration and sociability task; with the latter having the least. Therefore, a comparison of CCH peak lag for B6 putative pairs during cortex-linked executive tasks indicated a significant delay in the sociability tasks compared with the object exploration tasks (Figure 7M, $p=0.02$). For 129S CA1 ensembles, no significant change in CCH peak lag was observed between spatial and object exploration tasks (Figure 7N; $p=1$). However, the peak lag increased significantly for the sociability task ($p=0.02$), compared with the outcome for spatial exploration.

Feedback inhibition

B6 CA1 ensembles contained a significant percentage of putative pairs with positive CCH peaks and fewer with negative peaks. As expected, some putative pairs also appeared to be driven by a common input (Figure 7F). However, for 129S CA1 ensembles, a significant percentage of putative pairs were characterized by negative or dual CCH peaks depicting anatomically dominant feedback inhibition of the reference pyr cells (Figure 7H). These results suggested possible differences in 129S and B6 circuitry and might have indicated alterations in the interneuron innervation of pyr cells in the 129S CA1. B6 pyr/int pairs sampled during behavioral tasks involving cortical activation, compared with spatial exploration tasks, exhibited significant periods of inhibition (negative lags) for reverberating circuits (Figure 7O, obj $p=0.0014$; soc $p<0.0001$). Interestingly, no significant change was found in the negative CCH peak position for putative pairs in object exploration and sociability tasks ($p=1$). Similar to the CCH positive lags, behavior-specific alterations in the negative CCH lag time were observed in 129S pyr/int pairs. Here, the negative peaks for 129S putative pairs in object exploration tasks demonstrated prolonged inhibition states with respect to those in spatial exploration tasks (Figure 7P; $p=0.004$). However, the negative peaks observed during social interaction behavior did not significantly differ with respect to spatial ($p=0.3$) or object exploration scores ($p=0.2$).

In subsequent analyses, we determined the detectability index for excitatory and reverberating connection types by analyzing the z-score of the CCH peak mean. For excitatory connections (positive CCH peak) our results showed significantly higher z-scores for B6 pyr/int pairs object (Figure 7Q; $p<0.0001$) and social exploration (Figure 7R; $p<0.0001$) tasks, compared with spatial tasks. Interestingly, no significant change was observed in the z-score for 129S putative pairs across all behavioral tasks. Likewise, the z-score for 129S putative pairs was significantly lower than the B6 scores for spatial exploration ($p<0.0001$), object exploration ($p<0.0001$), and sociability ($p<0.0001$) tasks. A similar outcome was observed for reverberating B6 pyr/int pairs, in which the CCH mean z-score was significantly higher in the object (Figure 7R; $p<0.0001$) and social exploration tasks ($p=0.002$) than the spatial task. Furthermore, reverberating 129S pyr/int pairs did not show significant changes in the CCH mean z-score across behavioral tasks. A subsequent

comparison of B6 and 129S pyr/int pairs revealed a higher z-score for B6 reverberating putative pyr pairs for spatial exploration ($p=0.046$), object exploration ($p<0.0001$), and sociability ($p<0.0001$) tasks.

DISCUSSION

129S and B6 mice are among the most commonly used inbred strains in neuroscience research. Several transgenic lines and outbred strains have been developed from these individual strains or a combination of 129S and B6 lines. Generally, the 129S inbred lines bear significant mutations that could impair neural and cognitive function. A notable mutation in the 129S strain alters the *Disc1* gene and leads to the truncation of the DISC1 primary protein structure. Among other defects, the loss of *Disc1* function in the cognitive centers leads to incremental loss of excitation (N-methyl-D-aspartate receptor hypofunction) and spine dysgenesis (Arguello and Gogos, 2010; Clapcote and Roder, 2006; Malavasi et al., 2018; Moyer et al., 2015; Nakazawa et al., 2017; Ross et al., 2006). These neural changes underlie the various behavioral phenotypes attributed to 129S mice and other *Disc1* mutants used as schizophrenia and depression disease models (Arguello and Gogos, 2010; Ross et al., 2006; Wexler and Geschwind, 2011). Previous studies have shown that 129S and other *Disc1* mutants appear to be depressed, have reduced social interaction, and potentially exhibit some form of cognitive decline. In contrast, the C57BL/6 strain carries the wild-type *Disc1* gene and have typical behavioral phenotype (Brandon et al., 2009; Dittrich et al., 2017; Gomez-Sintes et al., 2014; Koike et al., 2006; Sauer et al., 2015). Together, the positive and negative behavioral symptoms associated with spontaneous *Disc1* mutation can lead to dysregulated excitatory and inhibitory function (Crabtree et al., 2017; Mesbah-Oskui et al., 2015; Sauer et al., 2015).

Although prior studies have emphasized excitatory neurons, recent studies have shown that firing patterns and distribution of fast-spiking interneurons in the hippocampus and prefrontal cortex are altered in *Disc1* mutant strains (Mesbah-Oskui et al., 2015; Sauer et al., 2015). At the network level, a loss of excitatory pyr cell activity and changes in the int (inhibitory cell) count underlie abnormal brain oscillation patterns, which are now considered endophenotypic for Disc1-related and other schizophrenia disease models. The current study assessed the firing properties of putative pyr cells and int in the CA1 in freely behaving 129S and B6 inbred mice. By comparing CA1 putative neuron properties for hippocampus and cortex-linked tasks, our results elucidated the significance of the loss of excitability in 129S CA1 neuronal ensembles. Specifically, 129S pyr and int units had lower FR scores than B6 neurons. Therefore, firing rate supression in putative 129S pyr and int followed task-specific patterns. Whereas 129S and B6 putative neurons showed similar ΔFR patterns for hippocampus-dependent spatial exploration and cortex-linked object exploration tasks, the discordant ΔFR outcomes were notable in 129S CA1 ensembles in sociability tasks.

Our results further demonstrated that the dysregulation of the pyr and int firing rate in 129S CA1 ensembles translated to delayed connection for putative pyr/int pairs in some cognitive tasks. Notably, significant delays were recorded in spatial exploration and sociability tasks, and an empirical increase in connection time was observed during object exploration

tasks. Generally, 129S putative pyr/int pairs were characterized by a significantly lower detectability index across all behavioral tasks. For the B6 pyr/int pair, the detectability index was significantly higher for cortex-linked executive tasks than the CA1-dependent spatial exploration task. In contrast, no significant change was observed for 129S pyr/int z-score mean (index). Together, our findings indicated that 129S mice exhibited significant cognitive decline attributable to a change in pyr cell excitability, and spike timing fidelity for pyr cell-driven int activity.

129S mice exhibit lower cognitive performance

Given that CA1 pyr cells' FR is strongly associated with the velocity of movement, we inferred that lower FR scores for 129S pyr cells in spatial exploration, object exploration, and sociability tests might have been a result of lower velocity and chamber exploration scores. Similar results were obtained for naive 129S mice without neural implants and 129S mice with neural implants (tethers). Of note, in spatial exploration tasks, the 129S mice explored the edges of the open field while avoiding the central area of the testing chamber (Figure 3K). This result likely indicates anxiety in the 129S inbred strain and was further evident during the object exploration (Figure 4H) and sociability tasks (Figure 5J). We observed that the 129S mice showed some level of activity at the beginning of a 300 sec task (Brown et al., 2004; Wolf et al., 2016), which was followed by periods of alternating activity and inactivity. Comparatively, B6 mice showed robust activity for the duration of these tasks. The decreased mobility and active time in 129S mice were consistent with findings from previous studies examining depression behavior in another *Disc1* mutant (LP100) strain (Sauer et al., 2015).

Decreased firing rate of putative pyr cells in the CA1 of Disc1 mice

DISC1 protein is directly associated with excitatory receptor function in hippocampal and cortical postsynaptic density. Our results indicated a spontaneous loss of DISC1 function in the brain of adult 129S mice, which was accompanied by significant suppression of pyr cell firing rate during learning. Thus, the mean FR (Hz) of putative pyr cells in the 129S CA1 ensemble was significantly lower than the FR of B6 pyr cells for all behavioral tasks. Furthermore, we observed variations in the mean FR for spatial exploration and executive behavioral tasks. B6 pyr cells showed significantly higher FR scores in CA1-dependent spatial exploration tasks than those for cortical executive functions (novel object and sociability tasks). However, for 129S pyr cells, we found that the mean FR was either not significantly different or lower when comparing FR scores for spatial exploration and executive cognitive tasks. Together, these results showed that local hippocampal activation of 129S pyr cells in spatial exploration tasks was significantly impaired, whereas the indirect cortical activation mechanism was dominant during executive cognitive tasks. Because putative pyr cells were characterized by ISI variability, regularity of firing for the pyr neurons was determined as the CV2 score. Given the low FR score for 129S pyr cells in CA1-dependent spatial exploration tasks, these cells exhibited significant ISI variability. Interestingly, for cortex-linked executive function, ISI variability was attenuated and was not significantly different from the B6 CV2 scores. This result supports the possible dominance of cortical activation over local hippocampal excitation mechanisms in 129S CA1 ensembles.

Since pyr cell firing is pertinent to int activation, the lower int FR scores for 129S int were likely to be associated with the diminished excitability of the pyr cells. As described previously for 129S pyr cells, the FR of 129S int units was also significantly lower than the B6 int FR scores (Figure 6). Impairment of pyr cell-driven int activation in 129S neuronal ensembles is further evident as significant variability in 129S int FR, which underscores the firing irregularity, derived as the CV score. In all behavioral tasks, 129S putative units showed significant FR and (or) ISI variability in comparison with B6 int units. Decreased pyr cell firing rate and a loss of excitability in the 129S CA1 was consistent with findings from previous studies demonstrating place cell abnormalities in the hippocampus in other *Disc1* mutant strains (Mesbah-Oskui et al., 2015). Therefore, a decrease in the pyr cell activation of int may underlie the decrease in int FR and firing irregularity in 129S CA1 neuronal ensembles.

Decreased fidelity of pyr cell-int monosynaptic pairing in 129S CA1

Hippocampal theta power is regulated by pyr cell-int monosynaptic pairing (Bender et al., 2015; Herweg et al., 2016; Mizuseki and Buzsaki, 2014; Soltesz and Deschenes, 1993; Tort et al., 2013). Consequently, the delayed pairing of putative CA1 pyr and int leads to the dysregulation of theta power, which is pertinent to hippocampal-cortical activity. Our results showed that the low FR scores for 129S putative pyr and int units caused a significant delay in pyr/int CCH peak lag for most cognitive tasks. Therefore, a lower fidelity of pyr/int pairing, on a millisecond time scale, for 129S pyr/int pairs was consistent with previous reports of abnormal gamma oscillations in a Disc1 mutant strain that recapitulates depression and defective working memory (Sauer et al., 2015). Defective pyr/int pairing has also been shown to impair the place cell firing rate resolution in freely moving mice with *Disc1* mutations (Mesbah-Oskui et al., 2015).

Analysis of neuronal connectivity and synaptic profiles revealed a predominant distribution of putative pairs with positive CCH peaks in B6 ensembles (Figure 7F) and reverberating (dual or negative) peaks for 129S ensembles (Figure 7H). Interestingly, based on CCH peak lag (synaptic profile) a similar distribution pattern was observed in B6 and 129S ensembles across behavioral tasks. The distribution of putative pairs with monosynaptic inputs (1.5–5 ms) decreased for cortical executive tasks, which were further characterized by an increase in pairs with transsynaptic (5.1–15 ms) or delayed connections (15.1–30 ms) (Figure 7G and 7I). Interestingly, the detectability index (z-score) for these putative pairs was significantly lower for 129S putative pairs than the B6 scores.

Analysis of B6 pyr/int pairs showed that the detectability index (z-score of the CCH peak) was higher for cortex-linked executive tasks than the CA1-dependent spatial exploration task. This finding was the case for putative pairs with positive (Figure 7Q) and negative peaks (Figure 7R), thus suggesting that cortical activation of CA1 putative pairs, compared with local hippocampal activation mechanisms, increases the detectability index. In contrast, the detectability index of the CCH did not significantly differ for 129S putative pairs for hippocampus or cortex-linked tasks. This finding illustrated poor pyr/int connectivity detection in 129S CA1 ensembles and might have resulted from suppressed excitability (burst) of the reference CA1 pyramidal cells during cognitive tasks (Figures 3Q, 4R, and

5R). This decreased FR and burst discharge for 129S pyr cells further underscores the delayed CCH peak lag for 129S pyr/int CCHs, because burst firing in pyr cells would increase int postsynaptic targeting and the probability of eliciting a response (Buzsaki et al., 2002; Harris et al., 2001; Terada et al., 2017). Based on these results, we inferred that the decrease in 129S putative int FR resulted from the decrease in pyr FR and weaker pyr/int monosynaptic pairing. This outcome is consistent with previous reports of impaired presynaptic excitatory innervation of postsynaptic int in the hippocampus of a *Disc1* mutant strain. Other significant findings included a decrease in the distribution of (Parvalbumin^{+} cells) and the dysregulation of GABAergic synaptic mechanisms in the hippocampus of a *Disc1* mutant strain. Ultimately, these studies have shown a decrease in presynaptic excitatory (pyr) input on postsynaptic int in the hippocampus of *Disc1* mutants (Kim et al., 2012; Mesbah-Oskui et al., 2015; Sauer et al., 2015; Xu and Wong, 2018).

Summary

In conclusion, mutations carried by the 129S inbred strain significantly impair the CA1 putative pyr cell firing rate and are predictive of diminished exploratory behavior during cognitive tasks. Dramatic changes in 129S pyr cell firing properties underlie the spike timing irregularity, which decreases the fidelity of pyr cell-int pairing during cognitive tasks.

Supplementary Material

Refer to Web version on PubMed Central for supplementary material.

Acknowledgments:

This work was funded by a CBS Bridging Grant (2020–2021) awarded to OOM. NIH grants R03MH104851, R03AG052120, R03AG056956, and R03NS109682 were awarded to CCL. IBRO-ARC Fellowship was awarded to APA.

Abbreviations

DISC1	disrupted-in-schizophrenia 1
CA	cornus ammonis (CA, as in CA1, CA3)
hil	hilus
int	interneuron
FR	firing rate (Hz or spikes/sec)
OFSS	offline spike sorting software
pyr	pyr cell layer or stratum pyramidal
ISI	interspike interval
CV	coefficient of variation (firing rate dependent)
CV2	coefficient of variation 2 (ISI dependent)

GABA	gamma-aminobutyric acid
ACG	autocorrelogram
CCH	cross-correlogram
VGAT	vesicular GABA transporter

References

Arancillo M, White JJ, Lin T, Stay TL, and Sillitoe RV (2015). In vivo analysis of Purkinje cell firing properties during postnatal mouse development. J Neurophysiol 113, 578–591. [PubMed: 25355961]

Arguello PA, and Gogos JA (2010). Cognition in mouse models of schizophrenia susceptibility genes. Schizophr Bull 36, 289–300. [PubMed: 20026558]

Bartho P, Hirase H, Monconduit L, Zugaro M, Harris KD, and Buzsaki G (2004). Characterization of neocortical principal cells and interneurons by network interactions and extracellular features. J Neurophysiol 92, 600–608. [PubMed: 15056678]

Basu J, and Siegelbaum SA (2015). The Corticohippocampal Circuit, Synaptic Plasticity, and Memory. Cold Spring Harb Perspect Biol 7.

Bender F, Gorbati M, Cadavieco MC, Denisova N, Gao X, Holman C, Korotkova T, and Ponomarenko A (2015). Theta oscillations regulate the speed of locomotion via a hippocampus to lateral septum pathway. Nat Commun 6, 8521. [PubMed: 26455912]

Bohbot VD, Copara MS, Gotman J, and Ekstrom AD (2017). Low-frequency theta oscillations in the human hippocampus during real-world and virtual navigation. Nat Commun 8, 14415. [PubMed: 28195129]

Bosch M, Castro J, Saneyoshi T, Matsuno H, Sur M, and Hayashi Y (2014). Structural and molecular remodeling of dendritic spine substructures during long-term potentiation. Neuron 82, 444–459. [PubMed: 24742465]

Brandon NJ, Millar JK, Korth C, Sive H, Singh KK, and Sawa A (2009). Understanding the role of DISC1 in psychiatric disease and during normal development. J Neurosci 29, 12768–12775. [PubMed: 19828788]

Brischoux F, Chakraborty S, Brierley DI, and Ungless MA (2009). Phasic excitation of dopamine neurons in ventral VTA by noxious stimuli. Proc Natl Acad Sci U S A 106, 4894–4899. [PubMed: 19261850]

Brown EN, Kass RE, and Mitra PP (2004). Multiple neural spike train data analysis: state-of-the-art and future challenges. Nat Neurosci 7, 456–461. [PubMed: 15114358]

Brown LY, Alexander GM, Cushman J, and Dudek SM (2020). Hippocampal CA2 Organizes CA1 Slow and Fast gamma Oscillations during Novel Social and Object Interaction. eNeuro 7.

Buzsaki G (2002). Theta oscillations in the hippocampus. Neuron 33, 325–340. [PubMed: 11832222]

Buzsaki G, Csicsvari J, Dragoi G, Harris K, Henze D, and Hirase H (2002). Homeostatic maintenance of neuronal excitability by burst discharges in vivo. Cereb Cortex 12, 893–899. [PubMed: 12183388]

Chazeau A, and Giannone G (2016). Organization and dynamics of the actin cytoskeleton during dendritic spine morphological remodeling. Cell Mol Life Sci 73, 3053–3073. [PubMed: 27105623]

Cho J, Bhatt R, Elgersma Y, and Silva AJ (2012). alpha-Calcium calmodulin kinase II modulates the temporal structure of hippocampal bursting patterns. PLoS One 7, e31649. [PubMed: 22363696]

Chung JE, Magland JF, Barnett AH, Tolosa VM, Tooker AC, Lee KY, Shah KG, Felix SH, Frank LM, and Greengard LF (2017). A Fully Automated Approach to Spike Sorting. Neuron 95, 1381–1394 e1386. [PubMed: 28910621]

Clapcote SJ, and Roder JC (2006). Deletion polymorphism of Disc1 is common to all 129 mouse substrains: implications for gene-targeting studies of brain function. Genetics 173, 2407–2410. [PubMed: 16751659]

Crabtree GW, Sun Z, Kvajo M, Broek JA, Fenelon K, McKellar H, Xiao L, Xu B, Bahn S, O'Donnell JM, et al. (2017). Alteration of Neuronal Excitability and Short-Term Synaptic Plasticity in the Prefrontal Cortex of a Mouse Model of Mental Illness. J Neurosci 37, 4158–4180. [PubMed: 28283561]

Diba K, Amarasingham A, Mizuseki K, and Buzsaki G (2014). Millisecond timescale synchrony among hippocampal neurons. J Neurosci 34, 14984–14994. [PubMed: 25378164]

Dittrich L, Petese A, and Jackson WS (2017). The natural Disc1-deletion present in several inbred mouse strains does not affect sleep. Sci Rep 7, 5665. [PubMed: 28720848]

Funahashi S (2017). Working Memory in the Prefrontal Cortex. Brain Sci 7.

Funahashi S, and Andreau JM (2013). Prefrontal cortex and neural mechanisms of executive function. J Physiol Paris 107, 471–482. [PubMed: 23684970]

Godsil BP, Kiss JP, Spedding M, and Jay TM (2013). The hippocampal-prefrontal pathway: the weak link in psychiatric disorders? Eur Neuropsychopharmacol 23, 1165–1181. [PubMed: 23332457]

Gomez-Sintes R, Kvajo M, Gogos JA, and Lucas JJ (2014). Mice with a naturally occurring DISC1 mutation display a broad spectrum of behaviors associated to psychiatric disorders. Front Behav Neurosci 8, 253. [PubMed: 25126062]

Harris KD, Hirase H, Leinekugel X, Henze DA, and Buzsaki G (2001). Temporal interaction between single spikes and complex spike bursts in hippocampal pyramidal cells. Neuron 32, 141–149. [PubMed: 11604145]

Herweg NA, Apitz T, Leicht G, Mulert C, Fuentemilla L, and Bunzeck N (2016). Theta-Alpha Oscillations Bind the Hippocampus, Prefrontal Cortex, and Striatum during Recollection: Evidence from Simultaneous EEG-fMRI. J Neurosci 36, 3579–3587. [PubMed: 27013686]

Hlushchenko I, Koskinen M, and Hotulainen P (2016). Dendritic spine actin dynamics in neuronal maturation and synaptic plasticity. Cytoskeleton (Hoboken) 73, 435–441. [PubMed: 26849484]

Jin J, and Maren S (2015). Prefrontal-Hippocampal Interactions in Memory and Emotion. Front Syst Neurosci 9, 170. [PubMed: 26696844]

Kaidanovich-Beilin O, Lipina T, Vukobradovic I, Roder J, and Woodgett JR (2011). Assessment of social interaction behaviors. J Vis Exp.

Kim JY, Liu CY, Zhang F, Duan X, Wen Z, Song J, Feighery E, Lu B, Rujescu D, St Clair D, et al. (2012). Interplay between DISC1 and GABA signaling regulates neurogenesis in mice and risk for schizophrenia. Cell 148, 1051–1064. [PubMed: 22385968]

Kobayashi R, Kurita S, Kurth A, Kitano K, Mizuseki K, Diesmann M, Richmond BJ, and Shinomoto S (2019). Reconstructing neuronal circuitry from parallel spike trains. Nat Commun 10, 4468. [PubMed: 31578320]

Koike H, Arguello PA, Kvajo M, Karayiorgou M, and Gogos JA (2006). Disc1 is mutated in the 129S6/SvEv strain and modulates working memory in mice. Proc Natl Acad Sci U S A 103, 3693–3697. [PubMed: 16484369]

Kvajo M, McKellar H, Arguello PA, Drew LJ, Moore H, MacDermott AB, Karayiorgou M, and Gogos JA (2008). A mutation in mouse Disc1 that models a schizophrenia risk allele leads to specific alterations in neuronal architecture and cognition. Proc Natl Acad Sci U S A 105, 7076–7081. [PubMed: 18458327]

Lai KO, and Ip NY (2013). Structural plasticity of dendritic spines: the underlying mechanisms and its dysregulation in brain disorders. Biochim Biophys Acta 1832, 2257–2263. [PubMed: 24012719]

Lee FH, Fadel MP, Preston-Maher K, Cordes SP, Clapcote SJ, Price DJ, Roder JC, and Wong AH (2011). Disc1 point mutations in mice affect development of the cerebral cortex. J Neurosci 31, 3197–3206. [PubMed: 21368031]

Li M, Long C, and Yang L (2015). Hippocampal-prefrontal circuit and disrupted functional connectivity in psychiatric and neurodegenerative disorders. Biomed Res Int 2015, 810548. [PubMed: 25918722]

Lueptow LM (2017). Novel Object Recognition Test for the Investigation of Learning and Memory in Mice. J Vis Exp.

Malavasi ELV, Economides KD, Grunewald E, Makedonopoulou P, Gautier P, Mackie S, Murphy LC, Murdoch H, Crummie D, Ogawa F, et al. (2018). DISC1 regulates N-methyl-D-aspartate receptor

dynamics: abnormalities induced by a Disc1 mutation modelling a translocation linked to major mental illness. Transl Psychiatry 8, 184. [PubMed: 30190480]

Mesbah-Oskui L, Georgiou J, and Roder JC (2015). Hippocampal place cell and inhibitory neuron activity in disrupted-in-schizophrenia-1 mutant mice: implications for working memory deficits. NPJ Schizophr 1, 15011. [PubMed: 27336029]

Mizuseki K, and Buzsaki G (2014). Theta oscillations decrease spike synchrony in the hippocampus and entorhinal cortex. Philos Trans R Soc Lond B Biol Sci 369, 20120530. [PubMed: 24366139]

Moyer CE, Shelton MA, and Sweet RA (2015). Dendritic spine alterations in schizophrenia. Neurosci Lett 601, 46–53. [PubMed: 25478958]

Nadel L, and Hardt O (2011). Update on memory systems and processes. Neuropsychopharmacology 36, 251–273. [PubMed: 20861829]

Nakahata Y, and Yasuda R (2018). Plasticity of Spine Structure: Local Signaling, Translation and Cytoskeletal Reorganization. Front Synaptic Neurosci 10, 29. [PubMed: 30210329]

Nakazawa K, Jeevakumar V, and Nakao K (2017). Spatial and temporal boundaries of NMDA receptor hypofunction leading to schizophrenia. NPJ Schizophr 3, 7. [PubMed: 28560253]

Ogundele OM, and Lee CC (2018). CaMKIIalpha expression in a mouse model of NMDAR hypofunction schizophrenia: Putative roles for IGF-1R and TLR4. Brain Res Bull 137, 53–70. [PubMed: 29137928]

Pastore VP, Massobrio P, Godjoski A, and Martinoia S (2018). Identification of excitatory-inhibitory links and network topology in large-scale neuronal assemblies from multi-electrode recordings. PLoS Comput Biol 14, e1006381. [PubMed: 30148879]

Penny CJ, and Gold MG (2018). Mechanisms for localising calcineurin and CaMKII in dendritic spines. Cell Signal 49, 46–58. [PubMed: 29847775]

Penzes P, Cahill ME, Jones KA, VanLeeuwen JE, and Woolfrey KM (2011). Dendritic spine pathology in neuropsychiatric disorders. Nat Neurosci 14, 285–293. [PubMed: 21346746]

Peyrache A, Dehghani N, Eskandar EN, Madsen JR, Anderson WS, Donoghue JA, Hochberg LR, Halgren E, Cash SS, and Destexhe A (2012). Spatiotemporal dynamics of neocortical excitation and inhibition during human sleep. Proc Natl Acad Sci U S A 109, 1731–1736. [PubMed: 22307639]

Phillips M, and Pozzo-Miller L (2015). Dendritic spine dysgenesis in autism related disorders. Neurosci Lett 601, 30–40. [PubMed: 25578949]

Ponce-Alvarez A, Kilavik BE, and Riehle A (2009). Relating firing rate and spike time irregularity in motor cortical neurons. BMC Neuroscience 10.

Ponce-Alvarez A, Kilavik BE, and Riehle A (2010). Comparison of local measures of spike time irregularity and relating variability to firing rate in motor cortical neurons. J Comput Neurosci 29, 351–365. [PubMed: 19449094]

Prescott SA, and Sejnowski TJ (2008). Spike-rate coding and spike-time coding are affected oppositely by different adaptation mechanisms. J Neurosci 28, 13649–13661. [PubMed: 19074038]

Quiroga RQ (2012). Spike sorting. Curr Biol 22, R45–46. [PubMed: 22280903]

Ranganath C, Heller A, Cohen MX, Brozinsky CJ, and Rissman J (2005). Functional connectivity with the hippocampus during successful memory formation. Hippocampus 15, 997–1005. [PubMed: 16281291]

Rebollo B, Perez-Zabalza M, Ruiz-Mejias M, Perez-Mendez L, and Sanchez-Vives MV (2018). Beta and Gamma Oscillations in Prefrontal Cortex During NMDA Hypofunction: An In Vitro Model of Schizophrenia Features. Neuroscience 383, 138–149. [PubMed: 29723576]

Ross CA, Margolis RL, Reading SA, Pletnikov M, and Coyle JT (2006). Neurobiology of schizophrenia. Neuron 52, 139–153. [PubMed: 17015232]

Sauer JF, Struber M, and Bartos M (2015). Impaired fast-spiking interneuron function in a genetic mouse model of depression. Elife 4.

Scheffer-Teixeira R, and Tort AB (2016). On cross-frequency phase-phase coupling between theta and gamma oscillations in the hippocampus. Elife 5.

Shao L, Lu B, Wen Z, Teng S, Wang L, Zhao Y, Wang L, Ishizuka K, Xu X, Sawa A, et al. (2017). Disrupted-in-Schizophrenia-1 (DISC1) protein disturbs neural function in multiple disease-risk pathways. Hum Mol Genet 26, 2634–2648. [PubMed: 28472294]

Shrestha A, Sultana R, Lee CC, Ogundele OM (2019). SK Channel Modulates Synaptic Plasticity by Tuning CaMKIIα/β Dynamics. Front Synaptic Neurosci. 2019 Oct 31; 11:18. doi: 10.3389/fnsyn.2019.00018. eCollection 2019. [PubMed: 31736736]

Soltesz I, and Deschenes M (1993). Low- and high-frequency membrane potential oscillations during theta activity in CA1 and CA3 pyramidal neurons of the rat hippocampus under ketamine-xylazine anesthesia. J Neurophysiol 70, 97–116. [PubMed: 8395591]

Spellman T, Rigotti M, Ahmari SE, Fusi S, Gogos JA, and Gordon JA (2015). Hippocampal-prefrontal input supports spatial encoding in working memory. Nature 522, 309–314. [PubMed: 26053122]

Stein IS, Gray JA, and Zito K (2015). Non-Ionotropic NMDA Receptor Signaling Drives Activity-Induced Dendritic Spine Shrinkage. J Neurosci 35, 12303–12308. [PubMed: 26338340]

Suresh J, Radojicic M, Pesce LL, Bhansali A, Wang J, Tryba AK, Marks JD, and van Drongelen W (2016). Network burst activity in hippocampal neuronal cultures: the role of synaptic and intrinsic currents. J Neurophysiol 115, 3073–3089. [PubMed: 26984425]

Swindale NV, Mitelut C, Murphy TH, and Spacek MA (2017). A Visual Guide to Sorting Electrophysiological Recordings Using 'SpikeSorter'. J Vis Exp.

Teng S, Thomson PA, McCarthy S, Kramer M, Muller S, Lihm J, Morris S, Soares DC, Hennah W, Harris S, et al. (2018). Rare disruptive variants in the DISC1 Interactome and Regulome: association with cognitive ability and schizophrenia. Mol Psychiatry 23, 1270–1277. [PubMed: 28630456]

Terada S, Sakurai Y, Nakahara H, and Fujisawa S (2017). Temporal and Rate Coding for Discrete Event Sequences in the Hippocampus. Neuron 94, 1248–1262 e1244. [PubMed: 28602691]

Tiesinga PH, Fellous JM, Jose JV, and Sejnowski TJ (2001). Computational model of carbachol-induced delta, theta, and gamma oscillations in the hippocampus. Hippocampus 11, 251–274. [PubMed: 11769308]

Tomoda T, Sumitomo A, Jaaro-Peled H, and Sawa A (2016). Utility and validity of DISC1 mouse models in biological psychiatry. Neuroscience 321, 99–107. [PubMed: 26768401]

Tort AB, Scheffer-Teixeira R, Souza BC, Draguhn A, and Brankack J (2013). Theta-associated high-frequency oscillations (110-160Hz) in the hippocampus and neocortex. Prog Neurobiol 100, 1–14. [PubMed: 23022096]

Tropea D, Hardingham N, Millar K, and Fox K (2018). Mechanisms underlying the role of DISC1 in synaptic plasticity. J Physiol 596, 2747–2771. [PubMed: 30008190]

Tropea D, Molinos I, Petit E, Bellini S, Nagakura I, O'Tuathaigh C, Schorova L, Mitchell KJ, Waddington J, Sur M, et al. (2016). Disrupted in schizophrenia 1 (DISC1) L100P mutants have impaired activity-dependent plasticity in vivo and in vitro. Transl Psychiatry 6, e712. [PubMed: 26756905]

Wang Q, Charych EI, Pulito VL, Lee JB, Graziane NM, Crazier RA, Revilla-Sanchez R, Kelly MP, Dunlop AJ, Murdoch H, et al. (2011). The psychiatric disease risk factors DISC1 and TNIK interact to regulate synapse composition and function. Mol Psychiatry 16, 1006–1023. [PubMed: 20838393]

Wexler EM, and Geschwind DH (2011). DISC1: a schizophrenia gene with multiple personalities. Neuron 72, 501–503. [PubMed: 22099453]

Woldeit ML, and Korz V (2010). Theta oscillations during holeboard training in rats: different learning strategies entail different context-dependent modulations in the hippocampus. Neuroscience 165, 642–653. [PubMed: 19896522]

Wolf A, Bauer B, Abner EL, Ashkenazy-Frolinger T, and Hartz AM (2016). A Comprehensive Behavioral Test Battery to Assess Learning and Memory in 129S6/Tg2576 Mice. PLoS One 11, e0147733. [PubMed: 26808326]

Wu Q, Li Y, and Xiao B (2013). DISC1-related signaling pathways in adult neurogenesis of the hippocampus. Gene 518, 223–230. [PubMed: 23353011]

Xu MY, and Wong AHC (2018). GABAergic inhibitory neurons as therapeutic targets for cognitive impairment in schizophrenia. Acta Pharmacol Sin 39, 733–753. [PubMed: 29565038]

Yamaguchi Y, Aota Y, Sato N, Wagatsuma H, and Wu Z (2004). Synchronization of neural oscillations as a possible mechanism underlying episodic memory: a study of theta rhythm in the hippocampus. J Integr Neurosci 3, 143–157. [PubMed: 15285052]

Zheng F, Wang L, Jia M, Yue W, Ruan Y, Lu T, Liu J, Li J, and Zhang D (2011). Evidence for association between Disrupted-in-Schizophrenia 1 (DISC1) gene polymorphisms and autism in Chinese Han population: a family-based association study. Behav Brain Funct 7, 14. [PubMed: 21569632]

Highlights

- The current study compares the firing rate (FR) of putative pyramidal cells or interneurons sampled in the CA1 of freely behaving B6 and 129S mice (inbred strains).
- FR score for 129S pyr and int units were significantly lower than B6 scores for similar behavioral tasks.
- Putative int in 129S CA1 ensembles show significant FR variability and high CV scores (irregular firing).
- Spike timing fidelity and detectability index were significantly lower for 129S CA1 putative pyr/int pairs.

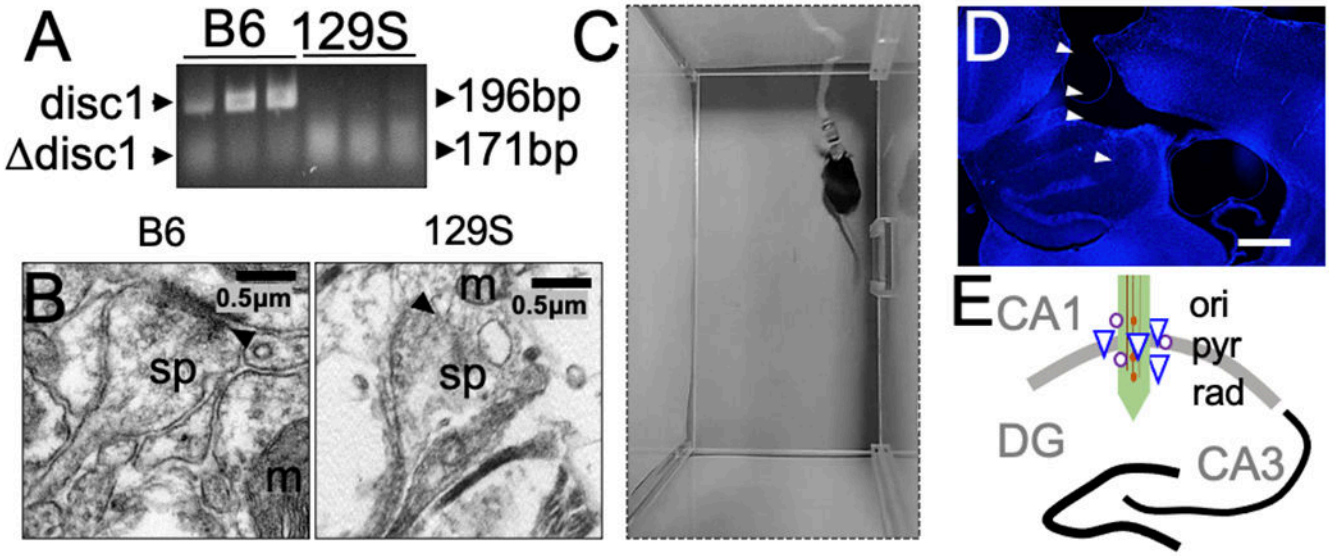

Figure 1: 129S mice exhibit spontaneous *Disc1* mutation.

A, Gel electrophoresis demonstrating the amplified *Disc1* gene in tail tissue biopsies of adult C57BL/6 and 129S mice. The mutant Disc1 gene in 129S mice shows truncation of the DNA sequence (179 bp) and decreased expression. The C57BL/6 strain expresses the wild-type *Disc1* gene (196 bp).

B, Transmission electron photomicrograph showing decreased synaptic fidelity in the hippocampus in 129S mice, compared with a normal synaptic profile in the C57BL/6 hippocampus. Scale bar=0.5 μm. sp: dendritic spine, m: mitochondria, and black arrowhead: postsynaptic density).

C, A mouse with a neural electrode implant, head stage, and a tethered SPI cable.

D, Representative fluorescence image showing DAPI counterstaining of a brain slice obtained from a mouse with an electrode implant (scale bar=0.5 mm).

E, Illustration of neural probe placement in the CA1 of a mouse. Here, a linear array is shown for demonstration purposes. Other experiments included four channel microelectrode arrays (ori: oriens layer, pyr: pyramidal cell layer, and rad: radiatum layer of the CA1).

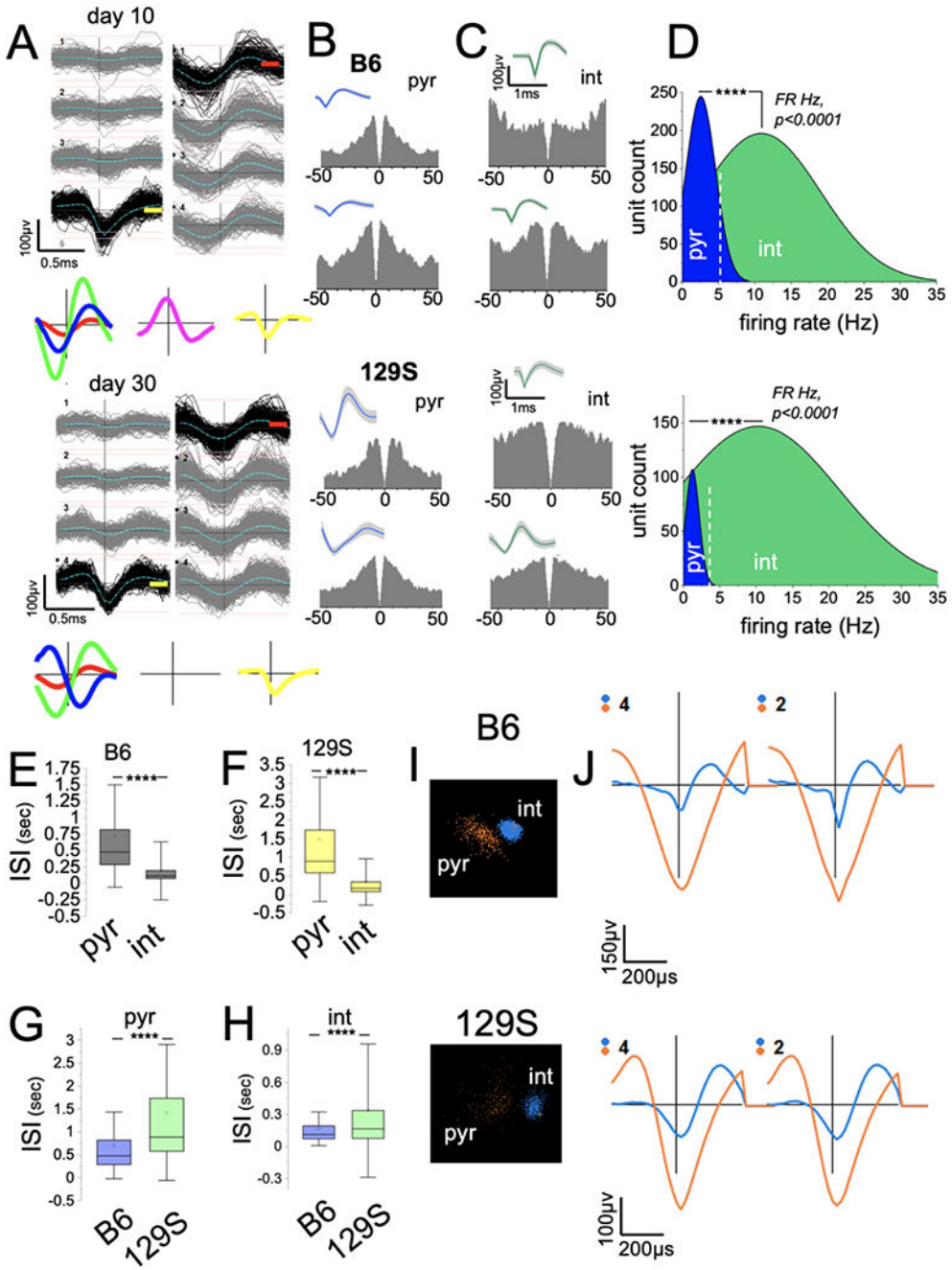

Figure 2: Detection of putative units in the CA1 in 129S and B6 mice.

A, PCA sorting of continuously recorded extracellular spikes demonstrating putative neuron clusters in the CA1 of a mouse after 10 and 30 days.

B-C, Sample autocorrelograms (ACGs; 0.5 ms bins) and waveform for putative pyramidal cell (B, pyr) and interneuron (C, int) units detected in B6 and 129S CA1.

D, Firing rate (FR Hz) distribution for neurons shows the clustering of ACG/waveform characterized putative pyr and int units (****p<0.0001, Mann-Whitney U test).

E-F, Graph illustrating higher ISI scores for putative pyr cells and lower ISI scores for int units in B6 (E, $p<0.0001$) and 129S (F, $p<0.0001$) CA1 ensembles (Mann-Whitney U test).
G-H, Graphs showing significantly higher ISI scores for 129S putative pyr (G, $p<0.0001$) and int (H, $p<0.0001$) units than for B6 putative units (Mann-Whitney U test).
I, Sample of putative pyr and int clusters in three-dimensional PCA clustering.
J, Waveforms corresponding to pyr and int waveform clusters.

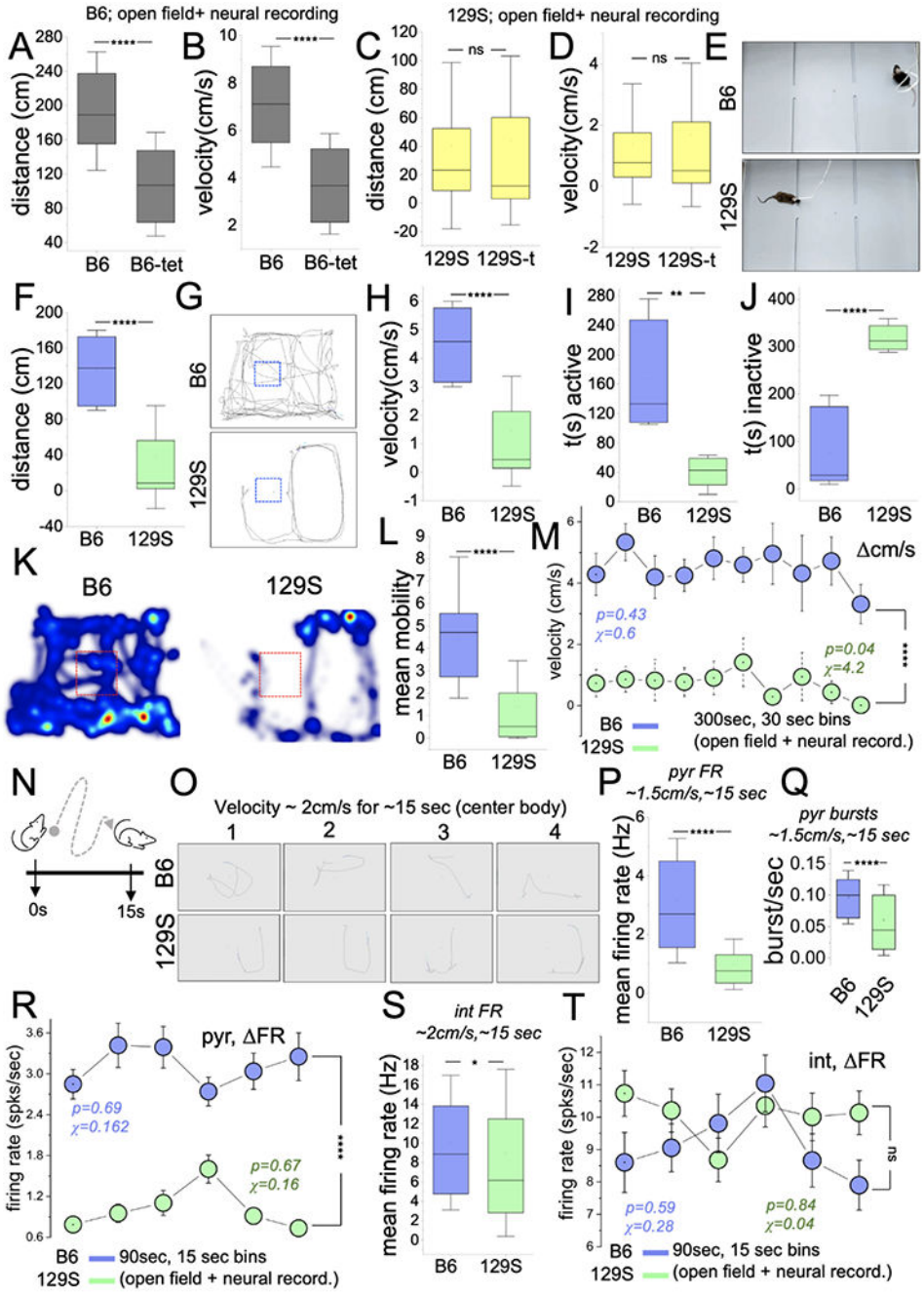

Figure 3: Lower exploration propensity is a characteristic phenotype of 129S mice.

A-B, Graphs depicting a decrease in the distance covered (cm, $p<0.0001$) and velocity (cm/s, $p<0.0001$) for B6 mice with neural implants and tethers (Mann-Whitney U test).

C-D, Graph illustrating no significant difference in distance (cm, $p=0.13$) and velocity (cm/s, $p=0.21$) for 129S mice with or without neural implants/tethers (Mann-Whitney U test).

E, Experimental setup for the open field task with extracellular recording in freely behaving B6 and 129S mice.

F, Graph comparing the mean distance for 129S and B6 mice in spatial exploration tasks (Mann-Whitney U test, $p<0.0001$).

G, Representative animal trail (center-body) depicting the total distance covered by a typical B6 and 129S mouse in an open field task.

H, Graph illustrating a lower mean velocity for 129S mice in open field tasks (Mann-Whitney U test, $p<0.0001$).

I-J, Graphs illustrating a lower activity duration ($p=0.001$) and higher inactivity duration ($p<0.0001$) for 129S mice (Mann-Whitney U test).

K, Representative heat maps demonstrating activity for a 129S mouse. Compared with the B6 mouse, the 129S mouse avoided the central area of the test chamber.

L, Graph showing lower mobility in open field tasks for the 129S group when compared with the B6 group (Mann-Whitney U test, p=<0.0001).

M, Comparisons of the velocity spread (Δcm/s) for 30-sec bins of open field (spatial exploration) tasks (two-way ANOVA, $p<0.0001$). B6 mice demonstrated robust exploratory behavior with sustained speed (chi-sq=0.6, $p=0.43$) for the task duration. 129S mice showed a significant decline in velocity, and a lower velocity score/bin for the open field tasks (chi-sq=4.2, $p=0.04$).

N, Cartoon illustration of a spatial exploration event during an open field test.

O, Sample of intervals with sustained exploration for a B6 and a 129S mouse.

P-Q, Graphs illustrating a low mean FR ($p<0.0001$) and burst rate ($p<0.0001$) scores for 129S putative pyr units, versus B6 putative units (Mann-Whitney U test).

R, Interval plot of FR (ΔFR) for putative pyr cells in open field tasks (two-way ANOVA, $p<0.0001$). Intervals depict six 15-sec bins for a 90-sec duration of exploration. The 129S pyr cells had low FR scores (spikes/sec) for the selected duration. No significant change was observed in ΔFR for B6 (chi-sq=0.162, $p=0.69$) or 129S (chi-sq=0.16, $p=0.67$) pyr neurons during open field tasks.

S, Graphs illustrating a lower mean FR for 129S putative int units during spatial exploration (Mann-Whitney U test; $p=0.02$).

T, Interval plot of FR (ΔFR) for putative int in open field tasks (two-way ANOVA, $p=0.06$). No significant change in ΔFR for B6 (chi-sq=0.28, $p=0.59$) or 129S (chi-sq=0.04, $p=0.84$) int was observed during open field tasks.

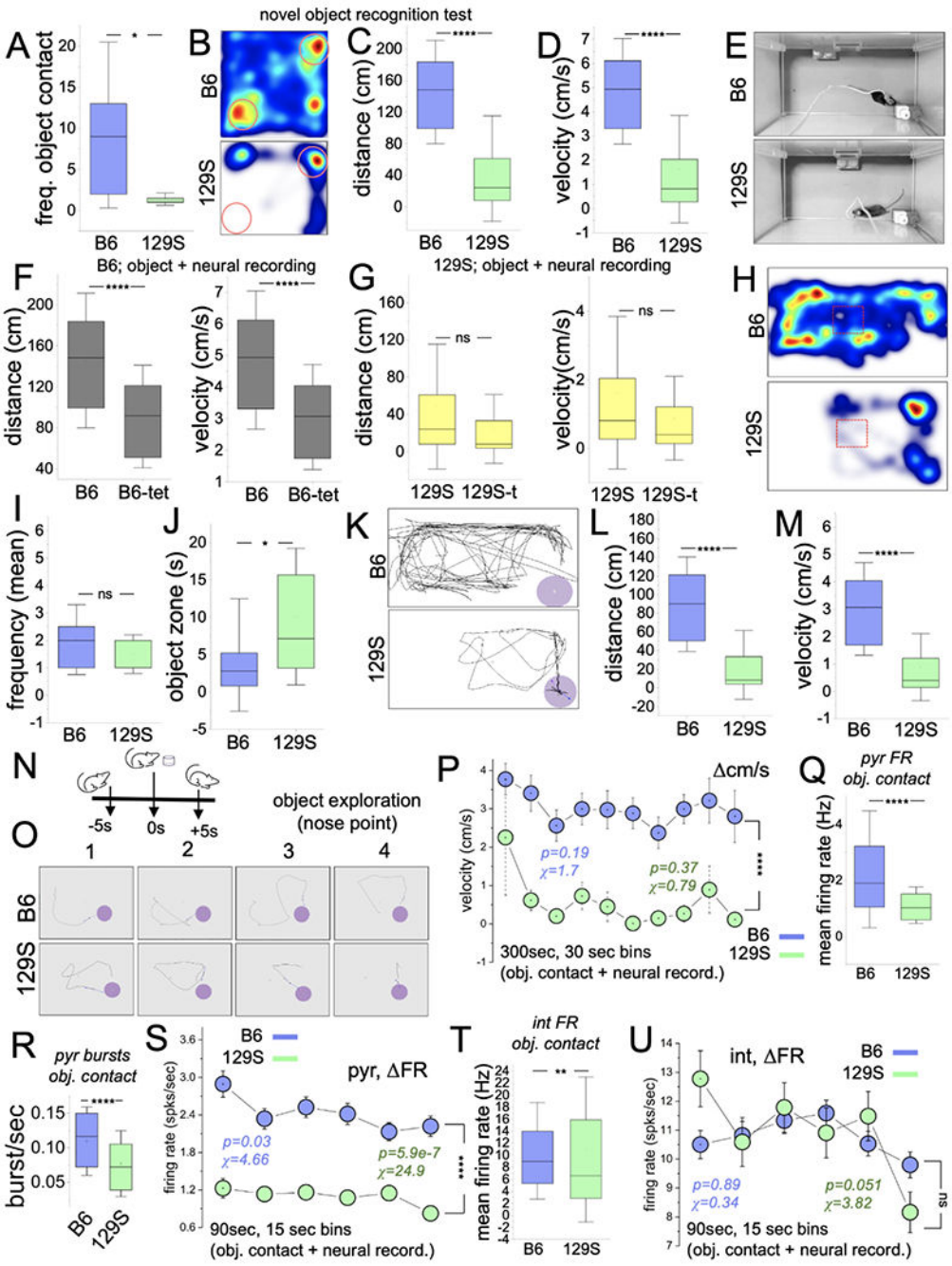

Figure 4: 129S mice exhibit a decline in object recognition memory

A, Graph illustrating a comparison of object exploration frequency for B6 and 129S mice without neural implants/tethers (p=0.02; Mann-Whitney U test).

B, Representative heat map illustrating mouse activity during a novel object recognition test.

C-D, Graph demonstrating a shorter distance (p<0.0001) and lower velocity (p<0.0001) for 129S mice (without neural implants/tether) in comparison to the B6 mice in a novel object recognition test (Mann-Whitney U test).

E, Experimental setup for an object exploration task combined with in vivo CA1 recording.

F, Graphs showing lower distance ($p<0.0001$) and velocity ($p<0.0001$) for B6 mice with neural implants/tethers versus B6 mice without neural implants (Mann-Whitney U test).
G, Graphs illustrating no significant change in exploration distance ($p=0.23$) and velocity ($p=0.23$) for 129S mice with or without neural implants/tethers.
H, Representative heat map showing exploration propensity for a B6 and a 129S mouse during object exploration tasks.
I-J, Graph illustrating the frequency of object contacts ($p=0.33$) and object zone duration ($p=0.014$) for B6 and 129S mice during object exploration tasks with neural recording (Mann-Whitney U test).
K, Representative mouse trail showing the distance covered by a tethered 129S or B6 mouse in an object exploration task.
L-M, Graph illustrating comparative distance ($p<0.0001$) and velocity ($p<0.0001$) for tethered 129S and B6 mice in an object exploration task (Mann-Whitney U test).
N, Cartoon illustration of an object exploration event.
O, Sample of intervals of object exploration for a B6 and a 129S mouse.
P, Interval plot of velocity spread (Δcm/s) for 30-sec bins of object exploration tasks (two-way ANOVA, $p<0.0001$). B6 (chi-sq=1.7, $p=0.19$) and 129S (chi-sq=0.79, $p=0.37$).
Q-R, Graphs illustrating a lower mean FR ($p<0.0001$) and burst rate ($p<0.0001$) scores for 129S putative pyr units in object exploration tasks (Mann-Whitney U test).
S, Interval plot of FR (ΔFR) for putative pyr cells in object exploration tasks. The 129S pyr cells had lower FR scores (spikes/sec) for the selected duration (two-way ANOVA, $p<0.0001$). ΔFR for B6 (chi-sq=4.66, $p=0.03$) or 129S (chi-sq=24.9, $p<0.0001$) pyr neurons decreased during the intervals of exploratory activity in object exploration tasks.
T, Graphs illustrating a low mean FR for 129S putative int units during object exploration ($p=0.006$).
U, Interval plot of FR (ΔFR) for putative int in object exploration tasks (two-way ANOVA, $p=0.61$). No significant change was observed in ΔFR for B6 (chi-sq=0.34, $p=0.89$) or 129S (chi-sq=3.82, $p=0.051$) int during object exploration tasks.

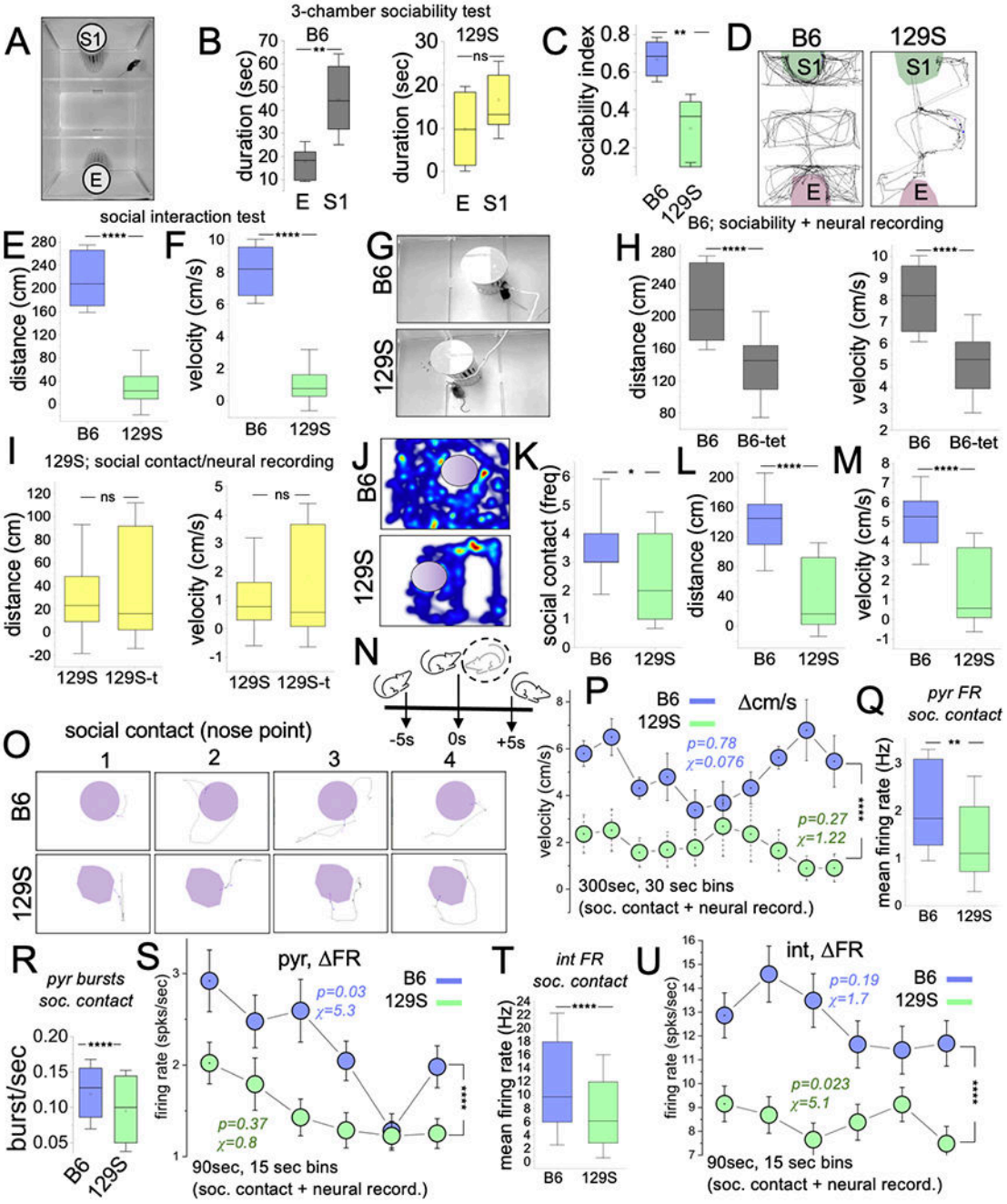

Figure 5: 129S mice show significant social deficits.

A, Three-chambered setup for a sociability test.

B, Graphs comparing the time spent exploring the empty and stranger mouse chambers for B6 and 129S mice in sociability tests. S1 was significantly higher for B6 mice (p=0.002). No significant difference was found between S1 and E for 129S mice (p=0.351, T-test).

C, Graph demonstrating a lower sociability index for 129S mice when compared with B6 mice (T-test, p=0.002).

D, Representative mouse trails comparing the exploratory activity for untethered 129S mice and B6 mice during sociability tasks.
E-F, Graph illustrating a lower distance (p=0.002) and velocity (mean) for untethered 129S mice during sociability tests (Mann-Whitney U test, p<0.0001).
G, Experimental setup for a sociability test in tethered 129S and B6 mice.
H, Graph showing significantly lower distance (p<0.0001) and velocity (p<0.0001) for tethered B6 mice than B6 mice without neural implants/tethers during the sociability task (Mann-Whitney U test).
I, Graph comparing the mean distance (p=0.30) and velocity (p=0.38) for tethered 129S mice with or without neural implants/tethers in the sociability task (Mann-Whitney U test).
J-K, Representative heatmaps, and graph illustrating the lower activity of 129S mice around the stranger mouse holding compartment. The frequency of social contact was lower for 129S mice than B6 mice (Mann-Whitney U test, p=0.014).
L-M, Graph illustrating the comparative mean distance (p<0.0001) and mean velocity (p<0.0001) for tethered 129S and B6 mice in sociability tasks (Mann-Whitney U test).
N, Cartoon illustration of a social contact event.
O, Sample of intervals for social contact bouts for a B6 and a 129S mouse.
P, Interval plot of velocity spread (Δcm/s) for 30-sec bins in sociability tasks (two-way ANOVA, p<0.0001). B6 (chi-sq=0.076, p=0.78) and 129S (chi-sq=1.22, p=0.27) mice exhibited sustained speed for the task duration. The velocity score for 129S mice was significantly lower for all intervals of the task.
Q-R, Graphs illustrating a low mean FR (p=0.0053) and burst rate (p<0.0001) scores for 129S putative pyr units in sociability tasks.
S, Interval plot of FR (ΔFR) for putative pyr cells in sociability tasks (two-way ANOVA, p<0.0001). The 129S pyr cells had low FR scores (spikes/sec) for the selected duration. ΔFR for B6 (chi-sq=5.3, p=0.03), and not 129S (chi-sq=0.8, p=0.37) pyr neurons decreased during the intervals of sociability tasks.
T, Graphs illustrating a low mean FR for 129S putative int units during sociability tasks (two-way ANOVA, p<0.0001).
U, Interval plot of putative int ΔFR in sociability tasks. No significant change in ΔFR was observed for B6 int (chi-sq=1.7, p=0.19). The 129S int change in FR significantly decreased for similar intervals of the same task (chi-sq=5.1, p=0.023).

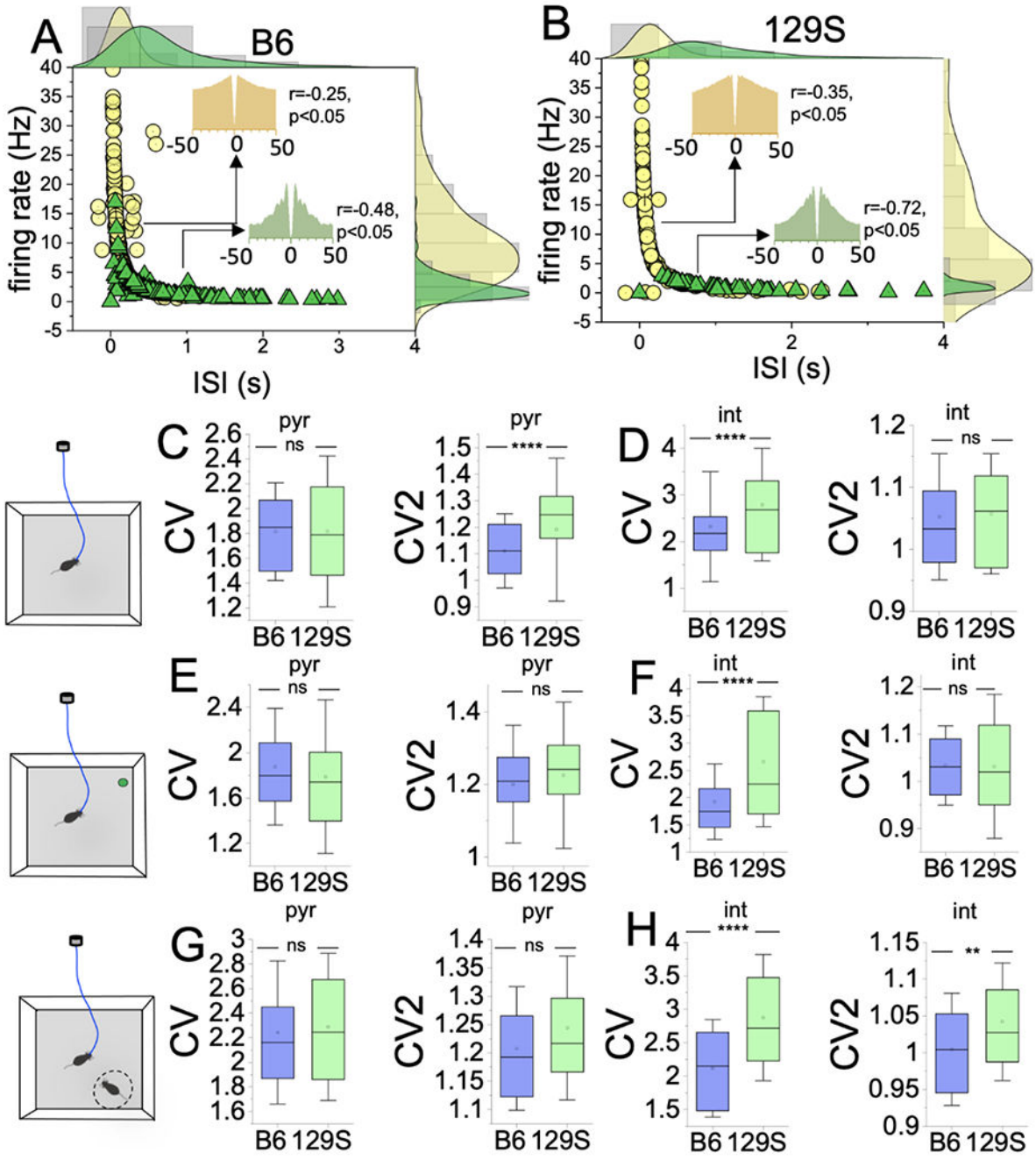

Figure 6: 129S mouse putative interneurons show significant FR variability and irregularity

A-B, Edge histograms demonstrating the clustering of putative pyr and int units based on mean FR (HZ) and ISI (sec) scores. Putative pyr cells show significant ISI variability, and int units show FR variability (Pearson's r).

Graphs comparing CV and CV2 scores for putative neurons detected in B6 and 129S CA1 during behavioral tasks (T-test).

C, Open field (spatial exploration task). The CV score was not significantly different for B6 and 129S putative pyr units (p=0.92). The 129S pyr cells exhibited higher CV2 scores than the B6 neurons (p<0.0001).

D, Spatial exploration task. The CV score was significantly elevated in 129S int versus B6 units (p<0.0001). The CV2 score was not significantly different (B6 vs 129S, p=0.44)

E, Object exploration: pyr CV (ns; p=0.11), pyr CV2 (ns; p=0.053).

F, Object exploration: int CV (p<0.0001), CV2 (ns; p=0.96).

G, Sociability tasks: pyr CV (ns; p=0.65), pyr CV2 (ns; p=0.17).

H, Sociability tasks: int CV (p<0.0001), CV2 (p=0.001).

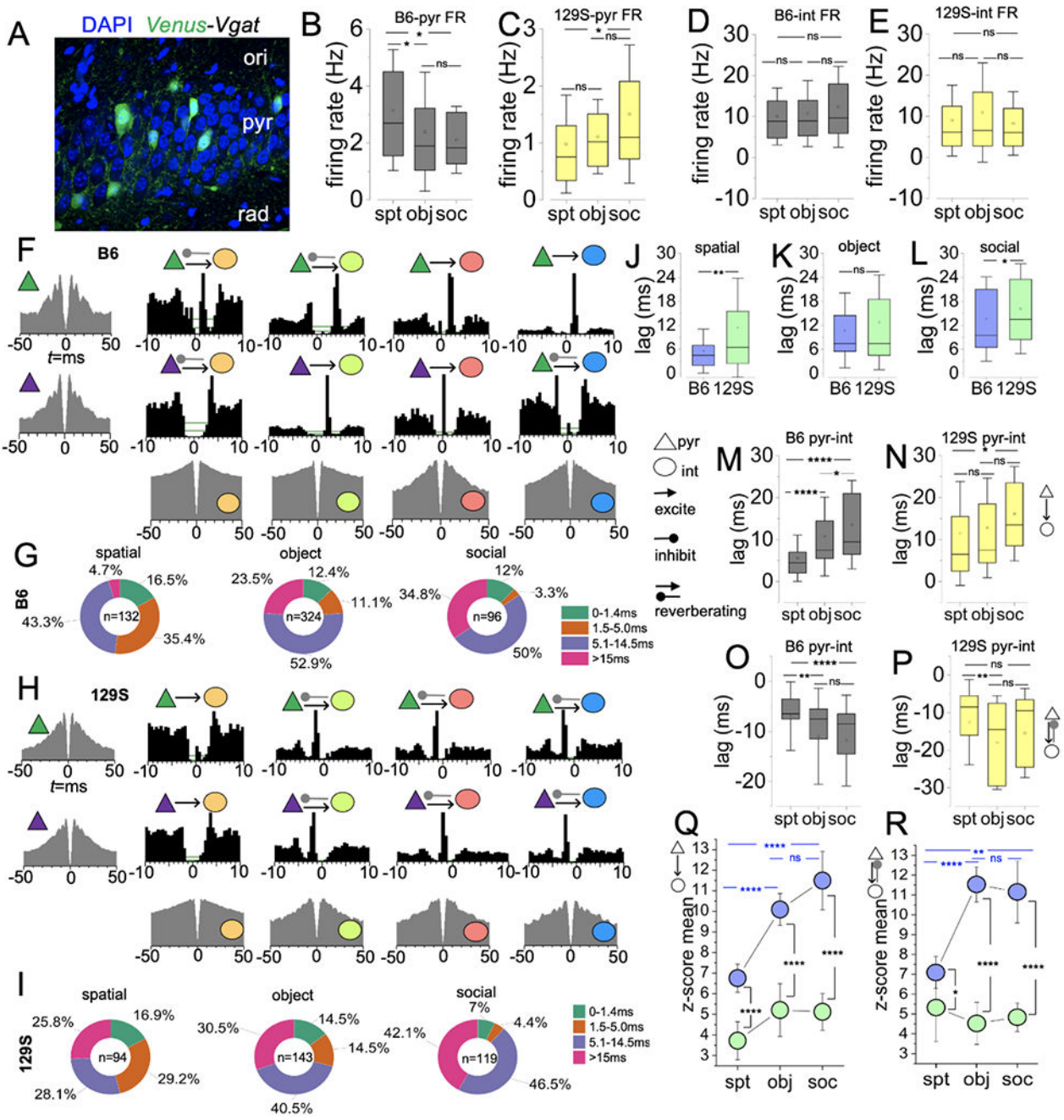

Figure 7: Cross-correlogram analysis of pyr/int putative pairs in 129s and B6 CA1 neuronal ensembles.

A, Fluorescence image demonstrating the distribution of VGAT^{+} cells (inhibitory GABA neurons) in the layers of the CA1.

B, Graph comparing the FR of B6 putative pyramidal cells across behavioral tasks (*one-way ANOVA*, spt vs obj: p=0.02, spt vs soc: p=0.05, obj vs soc: p=1).

C, Graph comparing the FR of 129S putative pyramidal cells (*one-way ANOVA*, spt vs obj: p=1, spt vs soc: p=0.01, obj vs soc: p=0.08).

D, Graph comparing the FR of B6 putative interneurons (*one-way ANOVA*, spt vs obj: p=1, spt vs soc: p=0.1, obj vs soc: p=0.2).
E, Graph comparing the FR of 129S putative interneurons (*one-way ANOVA*, spt vs obj: p=0.3, spt vs soc: p=1, obj vs soc: p=0.06).
F, ACGs (edge), and CCHs (inner) showing representative reference pyramidal cells and target interneurons in B6 CA1 neuronal ensembles.
G, Pie charts illustrating pairs with positive CCH peak, and the distribution of pyr/int pairs based on the lag (ms) of CCH peaks for B6 neuronal ensembles.
H, Representative ACG/CCH for 129S CA1 neuronal ensembles.
I, Pie chart depicting CCH peak lag distribution for pyr/int pairs in 129S CA1 ensembles.
J-L, Graph comparing positive CCH lag for B6 and 129S pyr/int pairs (average) during cognitive tasks (T-test); spatial p=0.007; object exploration p=0.34, and sociability p=0.04.
M, Graph comparing the mean CCH lag duration for B6 pyr/int pairs in cognitive tasks *(one-way ANOVA).* The decrease in monosynaptic connections for cortex-linked executive tasks agrees with a significant increase in CCH peak lag for object exploration ($p<0.0001$) and sociability tasks ($p<0.0001$), versus spatial exploration tasks. Similarly, dramatic reduction of monosynaptic inputs in sociability tasks, versus object exploration, is evident as an increase in CCH lag (p=0.02).
N, Graph comparing the mean CCH lag duration for 129S pyr/int pairs in cognitive tasks *(one-way ANOVA).* No significant difference in CCH peak lag for spatial vs object exploration task (p=1) and object exploration versus sociability task (p=0.08). CCH lag peak is significantly delayed for sociability tests in comparison with spatial exploration tasks (p=0.02).
O, Graph comparing negative CCH peak positions for B6 pyr/int pairs *(one-way ANOVA).* CCH peaks show prolonged inhibitory effects for reverberating pyr/int pairs in executive tasks in comparison with spatial exploration tasks (spt vs obj: $p<0.0001$, spt vs soc: p=0.001). There is no significant change in the negative CCH peak position for putative pairs in object exploration and sociability tasks (p=1).
P, Graph comparing negative CCH peak positions for 129S pyr-int pairs *(one-way ANOVA).* CCH peaks show prolonged inhibitory effects for reverberating pyr/int pairs in object exploration (p=0.004), and not sociability tasks (p=0.3), versus spatial exploration. There is no significant change in the negative CCH peak position for putative pairs in object exploration and sociability tasks (p=0.2).
Q, Graph comparing the mean z-score of excitatory CCH peak lags for B6 or 129S putative pyr/int pairs in cognitive tasks. *one-way ANOVA* (**B6:** spt vs obj, $p<0.0001$; spt vs soc, $p<0.0001$; obj vs soc, p=0.21 | **129S:** spt vs obj, p=0.3; spt vs soc, p=0.5; obj vs soc, p=1). Also, the graph compares B6 and 129S for specific behavioral tasks (*T-test*, spt, $p<0.0001$; obj, $p<0.0001$; soc, $p<0.0001$).
R, Graph comparing the mean z-score of reverberating CCH peak lags for B6 and 129S putative pyr/int pairs in cognitive tasks. *one-way ANOVA* (**B6:** spt vs obj, $p<0.0001$; spt vs soc, p=0.002; obj vs soc, p=0.2 | **129S:** spt vs obj, p=1; spt vs soc, p=1; obj vs soc, p=1). Also, the graph compares B6 and 129S for specific behavioral tasks (T-test, spt, p=0.046; obj, $p<0.0001$; soc, $p<0.0001$).